Trapped vorticity for controlled modification of an airfoil's aerodynamic loads

Daniel P. Brzozowski, Bojan Vukasinovic, and Ari Glezer

Phys. Rev. Fluids **4**, 034601 — Published 7 March 2019

DOI: 10.1103/PhysRevFluids.4.034601

Trapped vorticity for controlled modification of airfoil's aerodynamic loads

Daniel P. Brzozowski[1], Bojan Vukasinovic[2], and Ari Glezer[2]

[1]The Boeing Company

[2]Woodruff School of Mechanical Engineering, Georgia Institute of Technology

Abstract

The aerodynamic loads on a static airfoil are modified below its stall margin by deliberate formation and regulation of trapped vorticity on the suction and pressure surfaces near the trailing edge. Vorticity accumulation and shedding is effected using a hybrid actuator comprising a miniature 2-D passive protuberance having a cross-stream scale that is nominally commensurate with the local boundary layer thickness, and the vorticity flux is regulated using integrated spanwise arrays of equally-spaced high aspect ratio synthetic jet actuators. The aerodynamic loads are varied by independent differential control of flux of opposite sense vorticity from both sides of the airfoil that are characterized using measurements of the force/torque, surface pressure, and particle image velocimetry (PIV) over the suction surface and in the airfoil's near wake. The induced changes in circulation and lift and in the pitching moment are traced to complex, transitory changes in vorticity flux associated with the onset and termination of the actuation. These changes are characterized by transitory variations in the balance of flux and shedding of CW or CCW vorticity that is triggered respectively by actuation on the pressure or suction surfaces. These investigations indicate that hybrid flow control by trapped vorticity, which has the potential to manipulate pre-stall aerodynamic loads without mechanical control surfaces, may enable novel wing designs.

1. Introduction

The need for controlling the aerodynamic loads on lifting surfaces and bluff bodies has spurred significant interest in passive and active flow control strategies that have most commonly focused on mitigation of partial or full separation precipitated by adverse pressure gradients or by sharp surface discontinuities. Most commonly flow control strategies have exploited fundamental instabilities of the separated flow and relied on its narrow band receptivity to external actuation. The separation is simultaneously affected by two instability mechanisms namely, a local instability of the separating shear layer and, perhaps more importantly, a wake instability that ultimately results in the formation and shedding of large-scale vortical structures (e.g., Wu et al., 1998). Because the nominally time-periodic vortex shedding into the wake is accompanied by global changes in circulation, it is coupled to and strongly affects the evolution of the separating shear layer. In fact, this coupling appears to dominate the rollup of the shear layer whose inherent natural ('most unstable') frequency that scales with the local momentum thickness is typically higher than the global shedding frequency. Since the characteristic scale of the wake is typically commensurate with the scale of the separated flow domain, earlier works on separation control over fully-or partially-stalled airfoils has emphasized actuation frequencies that are on the order of the shedding frequency having a Strouhal number $St_{act} = L / U_c \, T_{act}$ of O[1]. In these approaches, the actuation period T_{act} is on the same order as the convective time scale T_{conv} over the separated flow domain (L and U_c are the characteristic advection length and speed, respectively). This approach to control of separation has been applied with varying degrees of success since the early 1980s to restore aerodynamic performance of stalled airfoils and flaps (e.g., Ahuja & Burrin, 1984; Hsiao et al., 1990; Seifert et al., 1993, Nishri &

Wygnanski, 1998, Buchmann, Atkinson & Soria, 2013). Actuation applied upstream of separation leads to the formation and shedding of vortical structures that scale with the length of the separated flow domain and the ensuing changes in the rate of entrainment result in a Coanda-like deflection of the separating shear layer towards the surface of the stalled airfoil such that the layer's vortices are effectively advected downstream in close proximity to the surface, as discussed, for example, by Glezer et al. (2005) and by Greenblatt (2006). A comprehensive review paper by Greenblat & Wygnanski (2000) discusses 'optimal' actuation frequencies (up to about $St_{act} \approx 4$) that appear to be better tune to the coupled receptivity of the near wake.

A different approach to the control of flow separation on lifting surfaces has emphasized fluidic modification of the "apparent" aerodynamic shape of the surface upstream of separation with the objective of altering the streamwise pressure gradient to achieve complete or partial bypass (or suppression) of separation. This change in aerodynamic shape is attained by the trapped vorticity resulting from interaction between fluidic actuation at much higher global actuation frequencies ($St_{act} >> 1$, typically $O[10\,T_{conv}^{-1}]$) and the cross flow above the surface. As demonstrated by Honohan et al. (2000) on a two-dimensional cylinder, the trapped vorticity interaction domain between a high-frequency synthetic jet and the cross flow over the surface displaces the local streamlines of the cross flow and thereby induces a 'virtual' change in the shape of the surface. The resulting change in the streamwise pressure gradient alters the evolution of the boundary layer and leads to a delay in separation. It is noteworthy that natural formation of a small, closed separation pocket (or bubble) near the critical Reynolds number of a cylinder allows the boundary layer to withstand higher than normal pressure rise and thereby delay separation (Roshko, 1993). Because "virtual" surface shaping utilizes actuation

frequencies that are high enough so that the interactions between the actuator and the cross flow is essentially nearly time-invariant on the global time scale of the flow (e.g., of vorticity shedding), it is effectively decoupled from the wake instability, leading to the modified aerodynamic forces, which tend to be time-invariant (Amitay & Glezer 2002b and Glezer et al. 2005). In addition, Cattafesta, Tian & Mittal (2008) argued that the disparate dominant flow scales would be effectively controlled if the control source excited all the relevant scales. They showed that such a nonlinear control approach significantly minimizes the necessary control input relative to linear approaches using an example of leading-edge flow separation over an airfoil.

This approach to separation control was demonstrated in several previous works in which control authority was achieved over a broad range of St_{act}. Amitay & Glezer (2002b) demonstrated high-frequency actuation on an unconventional airfoil and showed that the aerodynamic forces become almost invariant as the actuation frequency increases. Timor et al. (2007) used synthetic jet actuation to investigate 3D effects on a cropped NACA 0018 airfoil. Actuation led to a significant increase in lift and pitch-down moment particularly when the actuation phase was varied along the span. Watson et al. (2007) used high frequency actuation to control the separating shear layer over highly swept wings and thereby mitigate vortex breakdown and the resulting unsteady dynamic loading using an actuation frequency that was selected to be an order of magnitude above the characteristic vortex bursting frequencies. The actuation led to a reduction of about 40% in the unsteady pressures near the trailing edge.

In addition to the utilization of nominally time-stationary harmonic actuation, several investigations have considered anharmonic actuation to exploit transitory flow mechanisms that

are associated with the time-dependent flow evolution during separation and attachment. Amitay & Glezer (2002a, 2006) investigated flow transients associated with the onset and termination of high-frequency actuation that leads to flow attachment over a stalled airfoil, and noted the similarity to the transients that accompany separation and attachment during dynamic stall. In particular, Amitay & Glezer (2006) demonstrated that the separated flow is extremely susceptible to transitory actuation and showed that when the actuation input was applied on time scales that are significantly shorter than the characteristic advection time over the separated flow domain, the resulting aerodynamic forces are larger than the forces realized by conventional, continuous time-harmonic actuation. The onset and termination of continuous actuation over a flat-plate flap configuration were investigated by Darabi & Wygnanski (2004a,b) who reported similar characteristic attachment and separation times for 'optimal' actuation momentum coefficient C_μ and dimensionless frequency F^+. Siauw et al. (2010) investigated the transient attachment and separation on a NACA 0015 airfoil using fluidic vortex generators, and similarly, Mathis et al. (2009) considered transient attachment and separation by pneumatic disruption of an actuation jet which effects separation over a splitter plate when active. Recently, Siauw & Bonnet (2017) emphasized the significance of the transient activation and termination of the impulsive control of flow separation upstream from an airfoil's trailing edge. They also indicated that the transient termination event takes about twice the time of the actuation onset estimated to be $\Delta T^+ = \Delta(t \cdot U_\infty / L_{sep}) = 7.8$.

The utility of pulsed actuation for separation control was also demonstrated by Funk et al. (2002) and Crittenden & Glezer (2006) who used repetitive, momentary [O(1 ms)] high-impulse actuation jets produced by combustion-powered actuation. This work was later extended by

Brzozowski et al. (2010) to investigate transitory response of the flow over a stalled NACA 4415 airfoil to actuation by a single pulse having a characteristic time scale of $0.05T_{conv}$. These authors showed that the momentary actuation leads to a partial collapse of the separated flow domain, coupled with a momentary increase in circulation magnitude on a time scale that is nearly $10T_{conv}$. In subsequent investigation, Woo & Glezer (2013) demonstrated that successive actuation by single pulse or short actuation bursts results in a rapid build-up of circulation that can extend the streamwise domain of attached boundary layer towards the trailing edge. The fast dynamic response associated with the reattachment process, combined with the relatively long relaxation process, allows low duty cycle pulsed actuation bursts to prevent full stall between the bursts.

The use of flow control strategies in the absence of separation when the base flow is fully attached (e.g., at low angles of attack), and therefore the aerodynamic loads that can be effected are relatively small, has received considerably less attention. Potential applications include reduction of cruise drag, optimization of lift distribution, and trim for varying flight conditions. The aerodynamic loads are typically trimmed using the passive deployment of mechanical control surfaces (e.g., Smith 1975), or the small static and dynamic trailing edge 'Gurney' flaps (e.g., Liebeck 1978). However, an interesting approach was motivated by the notion that the circulation can be enhanced/reduced when vorticity concentrations become attached to the surface (e.g., Saffman & Sheffield 1977). The control of the aerodynamic loads by modifying the apparent shape of aero-surfaces using trapped vorticity concentrations is not new and was addressed in a substantial body of work in the 1940s and 50s. For example, Perkins & Hazen (1953) used a stationary, trapped vortex to alter the apparent local surface curvature and

therefore the direction of the external flow near the trailing edge of an airfoil to increase the lift at zero angle of attack. Although seemingly a simple approach in circulation control, it became clear that maintaining the vortex attached to the surface is a formidable task. The early work by Hurley (1959) considered improvements of low-speed characteristics of a nominally high-speed airfoil profile by introduction of a large forward flap that would trap a vortex over the leading suction side. In order to maintain 'free-streamline' attachment over the downstream flap surface (and full confinement of the vortex), he utilized steady jets over the leading Coanda surface. Another concept that relied on both upstream and downstream flaps for capturing multiple vortices to the airfoil surface without any active flow control was proposed by Kasper (Cox, 1973) and became known as the 'Kasper' airfoil. Rossow (1978) expanded on the application of the leading edge trapped spanwise vorticity by utilization of end-plate suction for the vortex stabilization, and reported lift coefficient of up to 10. More recently, Amitay et al. (2001) showed that the formation of a stationary trapped vortex above an airfoil at low angles of attack leads to reduction of pressure drag that is comparable to the magnitude of the pressure drag of the baseline configuration with minimal lift penalty. This approach was expanded later by DeSalvo & Glezer (2004) to manipulate the Kutta condition of an airfoil using controlled concentrations of trapped vorticity near the trailing edge by a miniature O[0.01c] hybrid actuator similar to a Gurney flap. The changes in the flow near the trailing edge result in significant global aerodynamic effects that include a substantial reduction in pressure drag (and therefore an increase in L/D_p) and a significant increase in the pitching moment. Traub & Agarwal (2008) and Shea & Smith (2009) showed that potential improvements in the performance of a passive Gurney flap can be realized by pairing it in a hybrid flow control configuration with a 2-D jet or

an array of synthetic jets, respectively. In a recent investigation, Feng, Choi & Wang (2015) explored the use of a DBD plasma actuator in place of a Gurney flap at low Reynolds numbers. Instead of actuation near the trailing edge, DeSalvo & Glezer (2005) realized a decrease in pressure drag with virtually no loss in lift or significant change in skin friction drag by trapping vorticity concentrations on the pressure surface near the leading edge. In a work that preceded the present investigation, DeSalvo & Glezer (2007) reported preliminary bi-directional changes in the pitching moment at low angles of attack without using moving control surfaces by using controllable, nominally-symmetric trapped vorticity concentrations on both the suction and pressure surfaces near the trailing edge.

The present investigations focus on the utilization of the trapped vorticity concentrations on both pressure and suction surfaces of an airfoil upstream of its trailing edge for direct manipulation of the trailing edge flow and Kutta conditions and thereby of the aerodynamic forces and moments when the base flow is nominally attached. Concentrations of spanwise vorticity are deliberately trapped and controlled by a small [O(0.01c)] passive surface protrusion coupled with a synthetic jet near its cross stream edge, as shown schematically in Figure 1. The present investigations focus attention on the underlying flow mechanisms that are associated bi-directional regulation (independently on the pressure and suction surfaces as depicted notionally in Figures 1a and c) of the vorticity flux and, consequently, the modifications of the aerodynamic loads.

2. Experimental Setup and Flow Diagnostics

The present experiments were conducted at the free stream velocity U_o = 30 m/s (Reynolds number of 870,000) in an open-return low-speed wind tunnel having a square test section measuring 92 cm on the side and 3 m long. The nominally constant cross-section 2-D wing

model is based on a NACA 4415 airfoil (Figure 2a) with a chord of c = 457 mm and maximum thickness to chord ratio of t/c = 0.15. The model, which spans the entire width of the wind tunnel test section, is comprised of multiple sections, each constructed of a fiberglass skin wrapped over an aluminum frame. The airfoil was not tripped using a conventional strip; instead, the leading edge skin had natural roughness that was deemed sufficient for tripping the flow. A stereo-lithographed (SLA) segment located between adjacent sections approximately at the midspan includes 73 static pressure ports and four high-frequency pressure sensors. Time-resolved surface pressure is measured at the leading edge, the trailing edge, on the suction surface (x/c = 0.39), and on the pressure surface (x/c = 0.4) using piezoresistive pressure sensors with a range of ±1 kPa and a resolution of ±10 Pa. The model is assembled around a hollow shaft that is used for installing it in the test section and mounting it on a dynamic 3-DOF (pitch, plunge, and roll) traverse (Brzozowski, 2011). In the present investigations, the model is held stationary at pre-set pitch angles α and is decoupled from the response of the flow field to the actuation by operating the pitch servo actuator in closed-loop using a PID controller. The airfoil's angle of attack is set by and controlled in closed loop using a simple, single-input-single-output PID controller using an angular encoder sensor and a servo motor actuator, respectively. It is noted that the controller, in fact, is not informed of the flow state or flow control actuation, and the commands to pressure- and suction-side flow control actuators are applied in 'open loop' using the laboratory computer. The present experiments also considered the dynamic response of the airfoil/controller to open-loop flow control actuation that effectively acts as a controlled aerodynamic disturbance. Clearly, this response is the airfoil's 'natural' aerodynamic response coupled with the pitching moment effected by the servo motor. These

investigations did not employ dynamic compensation. The pitch angle α was regulated by operating the pitch servo actuator in closed-loop. Naturally, as a result of the action of the pitch servo, the resultant time-dependent trajectory depends on the controller parameters. The torque applied to the servo during these maneuvers is given by

$$\tau_s(t) = k_{loop}[k_d\dot{\alpha} + k_p(\alpha - \alpha_o) + k_i\int_o^t(\alpha - \alpha_o)dt] + k_a\ddot{\alpha},$$

where α_o = 3° is the (constant) commanded pitch angle, k_{loop} is the "loop gain", $\{k_p; k_i; k_d\}$ are the usual PID gains, and k_a is an acceleration feedback gain. The acceleration feedback is used to compensate for the large inertia of the wind tunnel model. After a study for optimization of the airfoil recovery time after step transients (Brzozowski, 2011), the controller gains were set to k_a = 0 and k_{loop} = 30 for all of the experiments discussed in the present manuscript, where ideally infinitely large, k_{loop} was bound by the requirement for stable operation.

The traverse is instrumented with a number of sensors that allow for measurement of positions, velocities, and accelerations, as well as forces and moments. In the present experiments, the pitch angle is measured using a high-resolution optical encoder which is mounted on the pitch servo motor (a secondary angle measurement using an angular resolver is used to obtain the initial offset in pitch angle measurement). The accelerations, forces and moments are measured with a combination of linear and angular accelerometers, load cells and a calibrated torque servo (Brzozowski, 2011).

Bi-directional pitching moments on the airfoil model are effected by surface-mounted spanwise hybrid actuator modules that are each located some (adjustable) distance upstream of the trailing edge on the pressure- and suction surfaces of the airfoil model (*PS* and *SS*, respectively) as shown in Figures 2a and b. Each spanwise actuator module has a characteristic height of 0.017*c*

above the airfoil surface and is formed by an upstream-facing (0.13c long) ramp that houses an internal spanwise array of 17 equally-spaced synthetic jet actuators, each driven by a pair of opposite piezoelectric disks operating off resonance at f_{act} = 2,050 Hz. The actuator jet emanates from a rectangular spanwise slot 0.4 mm high and 33 mm long (parallel to the airfoil's trailing edge). The cylindrical Coanda surface downstream of the jet slot has a characteristic radius of 0.02c. The jet actuator in each array is operated synchronously, but the *SS* and *PS* actuators are driven independently to provide the equivalent of up/down flap deflections, respectively. The boundary layer thickness over the actuator's ramp clearly varies with the airfoil's angle of attack. For reference, the boundary layer thickness at the downstream edge of the ramp was assessed from the measurements to be 0.005c at $\alpha = 3^o$.

In the present experiments, it is convenient to introduce a single dimensionless parameter to describe the actuation state: $u_f = \varepsilon' \cdot \delta_{act}$, where $\delta_{act} = -1$ (*PS* actuation), 0 (no actuation), and +1 (*SS* actuation), where ε' is the fraction of the maximum operating voltage so that $-1 \le u_f \le 1$ with $u_f = -1$ and $u_f = 1$ corresponding to full *PS* and full *SS* actuation, respectively. Hot-wire measurements of the centreline jet speed, shown in Figure 3, exhibited a sinusoidal waveform having the same frequency as the driving signal and indicated that the RMS jet speed U_j at the actuator's orifice scales approximately linearly with the driving voltage, as shown in Figure 3a. The corresponding jet momentum coefficient $C_\mu = U_j^2 b_j / (U_0^2 c)$ shown in Figure 3b varies quadratically, from $C_\mu = 2\times10^{-4}$ at $\varepsilon' = 0.2$ to $C_\mu = 2\times10^{-3}$ at $\varepsilon' = 1$. The carrier waveforms of the *PS* and *SS* actuators (f_{act} = 2,050 Hz) are amplitude-modulated by $u_{f,SS}(t) = \min\{0, u_f(t)\}$ and $u_{f,PS}(t) = \min\{0, -u_f(t)\}$, respectively. The gains of the PID traverse controller (keeping a fixed pitch angle in response to the actuation) was adjusted using step actuation *SS* → *PS* and *PS*

→ *SS* in open loop.

The flow field over the airfoil is characterized using a time- and phase-averaged high-speed particle image velocimetry using micron-size seed particles injected into the tunnel through the trailing edge of a symmetric airfoil within the tunnel's plenum that is aligned vertically with the midspan plane $z = 0$. PIV images are acquired using a 1,024 × 1,024 pixel CMOS imager having a pixel spacing of 17 μm in both dimensions. At full resolution, the camera can record images at 1,000 fps which gives a maximum double-frame PIV sample rate of 500 Hz. In the present study, the camera is operated between 200 and 1000 fps. Typically, sets of 200 image pairs are recorded for time-averaged measurements or for each phase point in phase-averaged measurements (conditionally sampled relative to the actuation cycle). A multi-grid/multi-pass approach was used for the PIV processing. Three total passes were performed, with the first having a spot size of 64 x 64 pixels and the latter two having a spot size of 32 x 32 pixels. In both cases, interrogation regions were overlapped by 50%. Following each pass, a median filter was applied to remove spurious vectors. A subsequent correlation peak was replaced as the vector at that location if its median fell within three times the RMS of those neighbors. Following the first and second pass, all missing vectors were replaced via interpolation and a smoothing filter was applied. No interpolation or smoothing was applied following the final pass. Peak locking was mitigated by fitting a surface to the region immediately around peaks in the correlation plane during vector calculation. The spatial vector resolution was approximately 1.7 mm and 0.3 mm, respectively for the low- and high-resolution fields of view (the depth of field of the laser sheet optics was estimated to be 2 mm). The overall measurement uncertainty for the independent velocity components (u and v) was $0.09U_0$, or 2.7 m/s. The time-and phase-

averaged velocity data are used to compute the vorticity following the circulation method of Raffel *et al.* (2007).

The vertical force applied by the carriages on the pitch axis assembly is measured using a load cell mounted between the carriage and gimbals on either side of the tunnel, which are described in great detail by Brzozowski (2011). Finally, time-resolved surface pressure is measured at four points on the airfoil circumference at midspan using piezoresistive pressure sensors (*Honeywell*) having the frequency response over 10 kHz, which was sufficient to resolve time scales below the flow's convective time scale. These sensors have a range of ±1 kPa and a resolution of ±10 Pa and are located at the leading edge, the trailing edge, on the suction surface (x/c = 0.39), and on the pressure surface (x/c = 0.4).

3. The Aerodynamic Loads with Continuous Actuation

The time-averaged changes in aerodynamic loads effected by trapped vorticity concentrations that are engendered and manipulated using the suction- and pressure-side (*SS* and *PS,* respectively) actuators are assessed from measurements of the surface pressure about the midspan circumference of the airfoil. These measurements were obtained over a broad range of angles of attack $-5^o < \alpha < 15^o$ when *SS* and *PS* actuators (placed at $x/c = 0.86$ and 0.95, respectively) are inactive ($u_f = 0$), and when each is operating at full power (i.e., $u_f = 1$, or -1). Figures 4a-c show the pressure distributions for $\alpha = 3^o$, 9^o, and 15^o. These data show that the presence of the actuators on the pressure and suction surfaces has strong local and global effects on the pressure distribution that diminishes with increasing angle of attack. The presence of the inactive actuators leads to local reduction and increase in pressure on the suction and pressure sides, respectively, while having negligible effects for $x/c < 0.4$. Perhaps the most notable

feature of the modified airfoil is the decrease in trailing edge pressure (e.g., $C_p = -0.34$ at $\alpha = 3^o$) relative to the smooth airfoil due to the formation of a recirculation domain between the actuation jet exit plane and the trailing edge ($0.85 < x/c < 1$) which is discussed further in connection with the PIV measurements. Jet actuation on the suction and pressure surfaces leads to strong local suction peaks upstream of the trailing edge that are felt all the way through the leading edge that clearly modify the circulation domain. Furthermore, relative to the inactive actuator configuration, operation of the *PS* or *SS* actuators leads to a reduction or an increase in the magnitudes of the surface pressure, respectively, for $x/c < 0.6$. These observations are qualitatively consistent with the findings of DeSalvo & Glezer (2005, 2007) on a swept airfoil. The onset of stall on the suction surface of the smooth airfoil is evident by the local plateau downstream of 0.85c at $\alpha = 15°$ (Figure 4c, solid line). Clearly, the presence of the actuators alters the flow upstream of the trailing edge over both the pressure and suction surfaces (cf., Figure 4a). The separation upstream of the trailing edge and the associated thickening of the SS boundary layer for $\alpha > 10°$ diminish the effectiveness of the actuation, as shown in Figure 5e (at $\alpha = 15°$, $\Delta C_M < 0.01$).

The pressure distributions over the airfoil were integrated to yield the aerodynamic loads (lift, pitching moment and pressure drag), and the variations of the coefficients C_L, C_M and C_{Dp} with α are plotted in Figures 5a, b, and c, respectively, for the base airfoil and in the presence of the inactive and active actuators (full *SS*/*PS* actuation). In addition, the corresponding variation of these loads with actuation amplitude (relative to the unforced flow) are plotted in Figures 5d-f for $\alpha = 0^o$, 3^o, and 15^o. When the flow is fully-attached ($-5^o < \alpha < 10^o$), the presence of the inactive actuators results in a slight decrease in lift maximum $\Delta C_L = -0.04$ (5%) at $\alpha = 5^o$

(Figure 5a) that is accompanied by an increase in pressure drag $\Delta C_{Dp} = 0.015$ (27%) at $\alpha = 10^o$ (Figure 5b). As the base flow begins to separate for $\alpha > 10^o$ (as is evidenced by the gradual decrease in $\partial C_L/\partial\alpha$), the presence of the actuators appears to enhance the lift while the rate of pressure drag increase $\partial C_{Dp}/\partial\alpha$ is smaller than for the base airfoil (Figure 5b). It is noteworthy that for $\alpha < 10^o$, the inactive actuators have very little effect on the pitching moment (Figure 5b), and the pitching moment remains nearly invariant for $\alpha > 10^o$, while it begins to decrease in magnitude (less nose-down) for the base airfoil.

Operation on the *SS* ($u_f = 1$) and *PS* ($u_f = -1$) results in respective increment and decrement in lift relative to the base and unactuated airfoils over the full range of α (Figure 5a). The magnitude of the increase is nearly invariant ($\Delta C_L = 0.1$) when the flow is attached, but begins to decrease for $\alpha > 10^o$. This lift increment is accompanied by an increase in the magnitude of the nose-down pitching moment $-0.030 < \Delta C_M < -0.007$ for $-5^o < \alpha < 15^o$ (Figure 5b). Also, for $\alpha < 5^o$, the *SS* actuation mitigates some of the drag induced by the installation of the actuator, although this effect diminishes for $\alpha > 5^o$ owing to the increase in the lift-induced drag. The corresponding lift decrement effected by the *PS* actuator is $-0.18 < C_L < -0.21$ for $5^o < \alpha < 3^o$ and it remains invariant for $3^o < \alpha < 15^o$. This decrease in lift is accompanied by a substantial change in pitching moment across all angles (Figure 5b), with the largest increment at $\Delta C_M = 0.067$ at $\alpha = 12^o$. It is noteworthy that even the smallest increment ($\Delta C_M = 0.058$ at $\alpha = -5^o$ is larger than the changes effected by the *SS* actuator over the same range.

For sufficiently large *SS* and *PS* actuation ($0.2 < u_f < 1$), the lift and pitching moment vary nearly monotonically with u_f and the rate of change and attained magnitudes of C_L and C_M (Figures 5d and e, respectively) are higher on the pressure side, indicating that the actuation is

indeed more effective when the surface boundary layer upstream of the actuator is thinner. For this reason, the effectiveness of the actuation diminishes with α especially on the suction side. As already noted above, *SS* and *PS* actuation lead to a decrease in pressure drag (relative to the unactuated airfoil) (Figures 5c and f). In fact, for $\alpha > 3^o$,the pressure drag is *smaller* than for the smooth airfoil for full *PS* actuation. The earlier investigation of DeSalvo & Glezer (2007) indicates that the use of an isolated *PS* actuator near $0.2c$ can lead to a significant reduction in the global drag and compensate for the inactive actuators.

In the present investigation, the effects of the trapped vorticity concentrations on the aerodynamic loads are measured over ranges of actuator positions (x_{SS} and x_{PS}), actuation magnitudes, and angles of attack. These effects are analyzed using polar maps of the pitching moment (C_M) vs. the lift (C_L) which can be used to assess longitudinal aerodynamic stability as it relates to control forces required for changing trim or performing maneuvers that would be affected by such actuation. In these investigations, $0.83c < x_{SS} < c$, and $0.96c < x_{PS} < c$ (when x_{SS} or x_{PS} are equal to c the actuator is flush with the trailing edge), $-1 < u_f < 1$, and $-2° < \alpha < 10°$.

Figures 6(a-i) show the variation of ΔC_M and $\Delta C_{L,}$ or the increments in C_M and C_L relative to the base (smooth airfoil) in the presence of the inactive [Figures 6(a-c)] and active [Figures 6(d-i)] control. In Figures 6(a, d, g) the *SS* and *PS* actuators are flush with the airfoil's trailing edge, while in Figures 6(b, e, and f) the *SS* actuator is fixed at $x_{SS} = 0.88c$ and the *PS* actuator is moved within $0.96c < x_{PS} < c$, and in Figures 6(c, f, and i) the *PS* actuator is fixed at $x_{SS} = 0.98c$ and the *SS* actuator is moved within $0.83c < x_{SS} < c$ (the fixed actuator positions were selected based on earlier measurements that yielded a range that was deemed sufficient for pitch control). It should

be noted that the data in Figures 6(b, c, e, and f) are colored by the position of the moving actuators, while the data in Figures 6(e, f, h, and i) are colored by the magnitude of the actuation.

In the presence of the inactive actuators, ΔC_M varies nearly linearly with ΔC_L with negative slope [$(dC_L)/(dC_M) = -0.27$, indicating stability] over the range of angles of attack. When the position of the *SS* and *PS* actuators is varied and leads to variation in the extent of the trapped vorticity concentrations near the trailing edge, there is a simple offset in the pitching moment relative to the origin [6(b and c)] without an appreciable change in its stability slope. Moving the *SS* actuator upstream (starting from a position flush with the trailing edge) causes a decrease in the nose-down pitching moment (about $x = c/4$) for the same lift coefficient (Figure 6b). This is consistent with the airfoil's center-of-pressure moving upstream. Conversely, moving the *PS* actuator upstream corresponds to an increase in the nose-down pitching moment (Figure 6c), consistent with downstream motion of the center of pressure. In the presence of actuation, each of the curves in Figures 6(a-c) is simply extended linearly about five-fold compared to the effect of the range of actuators displacement (and of angles of attack). This significant extension indicates the sensitivity of the aerodynamic loads to the strength and scale of the trapped vorticity concentrations when they are manipulated by the actuation. These data clearly exhibit an asymmetric offset that favors actuation on the pressure surface owing to the thinner pressure surface boundary layer and the smaller angle between the surface flow over the actuator's ramp and the actuation jet which is affected by the airfoil's camber. The data from Figures 6(d-f) are reproduced in Figures 6(g-i), and are colored by actuation levels between full *PS* and *SS* actuation. As shown, the *PS* and *SS* actuations correspond to respective decrease and increase in lift and increase and decrease in nose-down pitching moment.

Finally, the increments in the lift and pitching moment are computed relative to the unactuated airfoil configurations ($\Delta\widehat{C_M}$ and $\Delta\widehat{C_L}$) using the *entire* set of the present data (about 3,000 points) so that the effects of the modifications of the base airfoil in terms of the different actuator positions are removed. As a result, the increments collapse onto a single line as shown in Figure 7 which captures the effects of the actuation and is centered about the origin for which the actuation vanishes. This collapse indicates that while the (invariant) slope is associated with the specific airfoil, the effects of the actuation depend primarily on the effects of the actuation on the trapped vorticity concentrations and the ensuing aerodynamic loads could be matched over different angles of attack without affecting the stability of the airfoil.

4. The Evolution of Trapped Vorticity Concentrations Near the Trailing Edge

The effects of the actuation on the structure and evolution of concentrations of trapped vorticity near the trailing edge that result in the global changes in aerodynamic loads discussed in §3 are investigated using PIV measurements in the midspan cross stream (x-y) plane of the airfoil. The *SS* and *PS* actuators are placed at $x/c = 0.86$ and 0.95, respectively for which the aerodynamic performance in terms of the effected changes in the pitching moment is deemed optimal. This optimal actuator configuration based on the streamwise location of the *PS* and *SS* actuator arrays was selected by considering the highest control authority as manifested by the largest effected changes in pitching moment for $1 < u_f < 1$ and a given free stream speed. The measurement domain is $0.84 < x/c < 1.07$ and $-0.07 < y/c < 0.12$ and includes the exit plane of the suction actuator jets [the trailing edge is located at $(x, y) = (c, 0)$]. It is noted that the pressure side actuator jets are obscured by the shadow of the airfoil. The instantaneous PIV measurements are

used to compute the time-averaged velocity field $\overline{u}$, the Reynolds stresses $\overline{u'u'}$, $\overline{v'v'}$, and $\overline{u'v'}$, and the time-averaged spanwise vorticity $\overline{\omega_z}$.

The effects of the actuation are assessed from raster plots of concentrations of the time-averaged spanwise vorticity $\omega_z \cdot c/U_0$ and velocity vectors at α = −3°, 3°, 9°, 15°, as shown in Figure 8 in the absence of actuation (Figures 8a-d), and for full *SS* ($|u_f| = 1$) and *PS* (u_f = -1) actuation (Figures 8e-h, and 8i-l, respectively). In the absence of actuation (Figures 8a-d), the base flow separates locally over the apex edge of the actuator (where the orifice of the synthetic jet is located) within the entire range of angles of attack. The separated flow is manifested by the formation of a shear layer that bounds a concentration of clockwise (CW) trapped vorticity within the closed recirculation domains downstream of the apex that extends beyond the trailing edge of the airfoil (Figures 8a-d). Although not fully-resolved, a similar concentration of counter-clockwise (CCW) vorticity forms on the pressure surface downstream of the *PS* actuator. Naturally, at higher α, the airfoil boundary layer upstream of the suction side actuators thickens and the vorticity in the shear layer over the actuator becomes more diffuse and is displaced away from the surface.

Activation of the suction-side actuators (Figures 8e-h) reduces the thickness of the CW vorticity layer downstream of the apex and consequently the characteristic scale of the trapped vortex. These changes result in a tilting of the flow downstream of the actuator towards the surface and in a reduction in the cross-stream width of the near wake. The downwash associated with the change in the topology of the trapped vorticity is accompanied by a pressure recovery downstream of the *SS* actuator as the flow attaches to the actuator's Coanda surface. While this reattachment is visible at all α, the shear layer exhibits a bifurcation with increasing α (in

particular, for α = 9° and 15°, Figures 8g and h, respectively). These data show two distinct regions of high concentration CW vorticity downstream of the jet. As the thickness of the surface vorticity layer on the actuator's ramp increases, the actuation only affects a thinner cross stream domain closer to the surface and this is the reason for the apparent bifurcation of the time-averaged vorticity distribution in Figures 8g and h. The lower layer is attached to the wall while the upper layer is advected parallel to the ramp but exhibits a cross-stream diminution of the vorticity towards the surface. The beginning of this bifurcation is visible for α = 3° (Figure 8e) in the slight CW vorticity depression at $(x, y)/c$ = (0.9, 0.05). These data suggest that at higher α, the increased suction between the *SS* actuator and the trailing edge is insufficient to entrain the entire width of the separating shear layer to the surface. The vorticity layer near the surface is associated with the propagation of the jet flow and appears to diminish with increasing α.

Activation of the pressure-side actuators (Figures 8i-l) causes the CCW trapped vorticity layer on the pressure side to become somewhat thinner and leads to an upwash of the near wake that is associated with a reduction in the lift and a nose-up pitching moment (relative to the unactuated airfoil). While in the data presented here the flow on the pressure side of the airfoil is blocked by the shadow of the airfoil, separate measurements (not shown) confirm that *PS* actuation results in local attachment between the actuator and the trailing edge that is similar to the effect of the *SS* actuator. In addition, it is noteworthy that pressure-side actuation results in significant changes in the trapped vortex upstream of the trailing edge on the suction side of the airfoil, and in migration of the stagnation point in the cross-stream direction from $\boldsymbol{x}/c$ = (1.06, 0) when u_f = 0 to $\boldsymbol{x}/c$ = (1.06, 0.02) when $u_f = -1$.

The vectoring or displacement of the flow that is effected by the actuation downstream of the airfoil's trailing edge is quantified by cross-stream distribution of vorticity flux at a given streamwise position in the near wake. For the time-averaged flow field, the local vorticity flux is computed as the product of the streamwise velocity and spanwise vorticity (neglecting turbulent stresses): $f_\omega = u \cdot \omega_z$. Cross-stream distributions of f_ω are extracted at $x/c = 1.05$ for a range of forcing levels $-1 < u_f < 1$ with increments $\Delta u_f = 0.1$ for $\alpha = -5°$, 3°, and 15° (Figures 9a-c, respectively). The traces on the plot are colored such that black corresponds to the unactuated flow and increasing levels of red (blue) correspond to increasing levels of *SS* (*PS*) actuation. While the cross-stream integral of the vorticity flux vanishes since the flow is steady, the distribution of the integrand is instructive for assessing the effect of the actuation on the flow structure in the near wake. In the absence of actuation ($u_f = 0$), the wake width, as may be defined by the cross-stream span between the positive and negative peaks of vorticity flux (black trace), varies from $0.055c$ at $\alpha = -5°$, to $0.062c$ at $\alpha = 3°$, to $0.088c$ at 15° (Figures 9a-c, respectively). Near $y = 0$ (the cross-stream elevation of the trailing edge), the flux exhibits a local inflection point which appears to be associated with reversed flow immediately downstream of the trailing edge (cf. Figures 8a-d) that is induced by the counter-rotating vorticity concentrations. Clearly, this reversed flow terminates at the stagnation point near the downstream edge of the airfoil, which, as indicated in Figure 8c and d, appears to migrate towards the pressure surface at higher angles of attack. The cross-stream distributions of f_ω also indicate that while at $\alpha = -5°$ the thicknesses of the vorticity layers on the pressure and suction sides are comparable, as α increases, the vorticity thickness on the suction side increases

significantly while on the pressure side it intensifies and becomes narrower as the favorable pressure gradient increases.

When the *SS* actuators (red traces) are operated at low power $0 < u_f < 0.2$, for $\alpha = -5°$ and 3° (Figures 9a and b, light red), the vorticity layer exhibits a slight cross-stream broadening, which is accompanied by an increase in the flux magnitude from either side. As the actuation level continues to increase, the magnitude of the peak decreases as the concentration of the CW vorticity is deflected downward (cf. Figure 8e-g) as the surface CW vorticity appears to wrap around the trailing edge (at $u_f = 1, f_\omega = 0$ is displaced to approximately -0.018*c* with respect to the unactuated flow). At $\alpha = 15°$ (Figure 9c) the flux distribution of the CW vorticity exhibits evidence of the bifurcation of the vorticity layer (Figure 8h) and is similar to the distribution of the unactuated flow even in full actuation power. This clearly indicates that the effects of the actuation diminish significantly when the flow over the suction surface is near stall (cf. Figure 5). The operation of the *PS* actuators (blue traces) leads to an *upward* deflection of the near-wake that increases monotonically with actuator power in Figures 9a-c. It is noteworthy that *PS* actuation leads to some cross stream deflection of the CW vorticity layer even at $\alpha = 15°$ (Figure 9c). However, as noted in connection with the load measurements (cf. Figure 5f), at $\alpha = 15°$ *PS* actuation appeared to *saturate* for $u_f < -0.5$. The flux traces exhibit a similar trend in that the vorticity layer from the lower side of the airfoil is displaced by 0.018*c* for $-0.5 < u_f < 0$ and only by 0.008*c* for $-1 < u_f < 0$.

A series of PIV measurements were captured phase-locked to the driving waveform of the *SS* actuator within the domain downstream of the orifice ($0.855 < x/c < 0.896$, $0.033 < y/c < 0.069$ the orifice is located at $x/c = 0.861$) at $\alpha = 3°$. In order to minimize the portion of the image

taken up by the airfoil model, the PIV camera was rotated along the pitch axis by 7.2° so that the actuator's ramp is approximately parallel to the top and bottom edges of the image. The data were acquired at 18 equally-spaced phases during the jet cycle, 20° apart. The jet actuation frequency is f_{act} = 2,000 Hz or a cycle period of $0.033 \cdot T_{conv}$ corresponding to a Strouhal number $St_{act} = f_{act} \cdot c/U_0 = 30.5$. The corresponding unsteady flow field is illustrated at phase increments of 80° in Figures 10a-e using color raster plots of the phase-averaged spanwise vorticity with overlaid velocity vectors. The sequence starts as the synthetic jet completes the previous suction half-cycle and begins the expulsion segment. As a result of the suction, the surface vorticity layer over the actuator's ramp is pulled toward the jet orifice (Figure 10a). Farther downstream, the vortex pair from the previous cycle is still visible at $\mathbf{x}/c = 0.88$. As the jet speed at the orifice increases, a counter-rotating vortex pair is formed near orifice that includes a dominant CW vortex that forms between the orifice and the adjacent surface (below), and a weaker CCW vortex that is weakened by the interaction with the CW vorticity layer above the orifice (Figure 10b). The CW vorticity begins to lift away from the surface as it is advected downstream and is accompanied by the CCW vortex (Figure 10c). As the cycle continues, the two vortices lift above the surface vorticity layer (Figures 10c and d) and are ultimately advected by the cross flow above the surface (Figure 10e) as the jet's suction cycle intensifies while the upstream vorticity layer once again wraps around the jet orifice. The balance between the blowing and suction cycles of the actuators is sufficient to keep the upstream vorticity layer attached to the Coanda surface and regulate the vorticity flux which, in turn affects the evolution of the trapped vorticity concentrations downstream of each of the *PS* and *SS* actuators (Figure 8) and consequently modify the flow around the trailing edge to alter the global aerodynamic loads

(increased lift and nose-down pitching moment associated with operation of the *SS* actuator). This formation of the vortex pair is nearly independent of the airfoil's angle of attack, its dynamics appears to be unrelated to the vorticity bifurcation seen in Figure 8.

The effect of the actuation on the flow field immediately downstream of the *SS* actuator is assessed in terms of the change in local circulation Γ_{CV} within the measurement domain. The total circulation within the domain is computed using the line integral $\Gamma_{CV} = \oint \mathbf{u} \cdot d\mathbf{l}$. In the absence of actuation, the circulation in this region is $-0.04 \cdot U_0 \cdot c$ (denoted by the black dashed line in Figure 10). When actuation is applied, the time-averaged local circulation increases to $-0.053 \cdot U_0 \cdot c$ which is consistent with the intensification of the CW vorticity layer over the surface downstream of the actuator. The variation in phase-averaged local circulation during the synthetic jet cycle is also shown in Figure 10. For $0 < \varphi < 80°$, Γ_{CV} increases in magnitude above the time-averaged level due to the strong CW vorticity build up at the jet exit during the suction segment of the actuation cycle (cf. Figures 10a-e). Following a peak local circulation of $-0.055 \cdot U_0 \cdot c$ at $\varphi = 80°$, this vortex pinches off and is advected downstream. As a CCW vortex develops between the first vortex and the jet exit, the local circulation decreases ($120° < \varphi < 200°$) below the time-averaged value before recovering ($200° < \varphi < 360°$), as the vortex pair flows out of the measurement domain. As shown in Figure 9, the flux of vorticity varies with the magnitude of the actuation, thereby enabling direct regulation of the circulation and therefore of the aerodynamic loads on the airfoil.

5. Transitory Trapped Vorticity Control

Understanding the characteristic time scales associated with the response of the trapped vorticity

concentrations to transitory actuation is crucial for implementation of real-time control. In this section, the characteristic response to step transitions between three states, namely unforced, full *SS* actuation, and full *PS* actuation ($u_f = 0, 1, -1$, respectively) are investigated. The response of the flow over the airfoil to the manipulation of the trapped vorticity concentrations is assessed from measurements of the flow field and of the time-dependent global aerodynamic loads (accounting for the rigid body dynamics of the model). The transient aerodynamic loads on the airfoil are measured using the support system as in the steady actuation considered in §§3 and 4. Following transitory actuation, the model undergoes small excursions in pitch and therefore the system that controls the airfoil's pitch angle is designed to be sufficiently damped so that that the aerodynamic response is quasi-steady having the same loads as the static airfoil at the same angle of attack (Brzozowski, 2011). In the present experiment, the model is held at $\alpha = 3^o$ and its servo actuator is adjusted so that step changes in actuation input yield a maximum excursion of $\Delta\alpha = \pm 3^o$. Repetitive actuation between *PS* and *SS* states or maximum nose-down ($u_f = 1$) to maximum nose-up ($u_f = -1$) pitching moment and vice versa is demonstrated in Figure 11. Starting with the stationary model with $u_f = -1$, the actuation input it switched to $u_f = 1$ at $t = 0$ and then back to $u_f = -1$ at $t = 328T_{conv}$. The resulting temporal variation in the induced aerodynamic moment and lift increments $\Delta C_M(t)$ and $\Delta C_L(t)$, respectively, and in the angle of attack $\alpha(t)$ are phase-averaged over 100 actuation cycles and are plotted using green traces in Figures 11a-c, respectively, along with the corresponding static values at the same angles of attack (cf. Figure 5). In response to the onset of actuation there is a rapid change in the induced aerodynamic pitching moment and lift that are the result of the changes induced by the trapped vorticity concentrations near the trailing edge. As discussed in connection with the unsteady

pressure measurements (Figure 12) below, these changes are imposed within 4-6T_{conv} before there is a significant change in α. The peak changes in C_M and C_L are -0.08 and 0.33, respectively. As a result of the induced C_M, α decreases and therefore the induced C_L and C_M change following the slow changes in in α (the peak excursion is reached at about 30T_{conv} following the onset of the actuation), until the support system restores the model to the nominal $\alpha = 3^o$ after about 200T_{conv}. It is important to note that this time scale is entirely dependent on the large inertia of the experimental model relative to the pitching moment provided by the actuated flow. On an actual flight vehicle using this actuation scheme, the inertia would be much lower relative to control authority. The response of the flow over the airfoil is assessed using time-resolved measurements of the surface pressure at four streamwise positions. Figures 12a-d show the time history of pressure changes ΔC_p (relative to the time-averaged pressure at $\alpha = \alpha_o$) at the leading edge (12a), on the suction surface at x/c = 0.39 (12b), on the pressure surface at x/c = 0.4 (12c), and at the trailing edge (12d). Based on the time histories of ΔC_L and ΔC_M during the transient actuation in Figure 11, ΔC_p tracks the same trend as the corresponding static levels for all time except perhaps during a few T_{conv} following each transition. The transient responses in Figures 11 and 12 clearly comprise the airfoil's 'natural' aerodynamic response coupled with the pitching moment effected by the servo motor driven by the PID controller (as marked by the green traces). For reference, these figures also show the corresponding traces for the static response of the airfoil model at the same angles of attack and actuation levels (black curves) which were tabulated in a look-up table separately. Considering that the slow characteristic response times in Figures 11 and 12 are indeed dominated by the PID controller, it is argued that the difference between the two curves is representative of the aerodynamic effects effected on

the airfoil's convective time scale. It is remarkable, that although the actuation is applied near the trailing edge, the upstream sensors (Figure 12a-c) exhibit convergence to quasi-steady levels within 2-4T_{conv}, while the trailing edge sensor (Figure 12d) converges within 1-2T_{conv}. For comparison, Darabi and Wygnanaski (2004) reported a minimum reattachment time 16T_{conv} for a fully separated flow over a flap ($c = L = 240$ mm), with initial transients complete after about 7T_{conv}. As the separated flow domains become shorter, so are the corresponding transient responses. Siauw et al. (2017) reported characteristic reattachment time of 2.3T_{conv} for the base flow separated over the last 30% of the NACA 0015 airfoil's chord ($c = 0.35$ m, $\alpha = 11^{o}$). Finally, in the present experiments, the domains of interest near the trailing edge are even shorter, as are the corresponding transient time scales (1-2 T_{conv}). Following the *PS-SS* transition, a sharp suction peak (C_p = -0:63) is evident at the trailing edge at t + 0:33T_{conv} that is associated with the shedding of a large-scale vortex at the trailing edge as the direction of the actuation changes. Following the *SS-P*S transition, a pressure peak (C_p = -0.45) is evident at the trailing edge at $t = 0.5T_{conv}$ (Figure 12d). Since this peak occurs immediately following the onset of *SS* separation at the trailing edge, this pressure spike is most likely associated with the sudden exposure to the slow fluid of the recirculation region downstream of the *SS* actuator when the jets are inactive. For the upstream sensors (Figure 12a-c), the same essentially monotonic convergence to steady state is evident as for the transition *PS-SS*. A short leveling of the C_p response at about t/T_{conv} = 380 in Figure 12c is noted, but not explored further, as deemed of secondary importance.

The response of the flow to the transient actuation was further characterized with phase-locked PIV measurements in the near wake. Phase-averaged maps of concentrations of the spanwise

vorticity $\hat{\omega}$ following the *PS*-*SS* and *SS*-*PS* transitions at $t/T_{conv} = 0.3$, 0.33, and 0.36 are shown in Figures 13a-c and 13d-f, respectively. The vorticity layer downstream of the actuators appears to bifurcate into two branches due to the train of CW vortices formed by the *SS* actuator. The CCW vortex which is visible on the right of Figure 13a at $x/c = (1.03, 0)$ results from the shear layer off the *PS* actuator as the CW vortex associated with onset of the *SS* actuation passes above it. This stronger interaction between the shear layers over the *SS* and *PS* actuators is due to the fact that at $t = 0.3T_{conv}$ the *PS* shear layer is vectored upward due to the *PS* actuation. The phase-averaged maps of $\hat{\omega}$ following the *SS*-*PS* transition (Figure 13d-f) show that at $t/T_{conv} = 0.3$, a large CCW vortex is present below and just downstream of the trailing edge [$x/c = (1.01, -0.02)$]. This vorticity concentration results from the *PS* shear layer that is severed by the onset of *PS* actuation, after which it rolls up and is advected downstream. For $0.33 < t/T_{conv} < 0.36$, this vortex moves downstream to $x/c = (1.05, -0.03)$ at an approximate speed of $0.63U_0$ (Figures 13b and c). Because the changes in the flow due to the termination of actuation have not propagated to the trailing edge by this time, there is little opportunity for the CCW vortices associated with the *PS* transition to interact with the *SS* shear layer.

Figures 13g–i and 13j–l show raster plots of the normalized spanwise vorticity $\hat{\omega}_z$ at three characteristic instances $t/T_{conv} = 0$, 0.07, and 0.46, following the transitions $0 \rightarrow SS$ and $SS \rightarrow 0$, respectively. At the onset of the transition $0 \rightarrow SS$ ($t = 0$, Figure 13g), the flow structurally corresponded to the time-averaged unforced flow (Figure 8b). At $t = 0.07T_{conv}$, the shear layer is pinched off (Figure 13h) and a CW vorticity concentration rolls up and is advected downstream. Meanwhile the upstream portion of the shear layer attaches around the Coanda surface downstream of the jet exit. As the large CW vortex grows and passes the trailing edge, a shear

layer reforms downstream of the actuator, as the flow attaches along the Coanda surface and the surface of the airfoil. By $t = 0.46T_{conv}$ (Figure 13i), the passage of the large vortex is complete and the flow nearly transitions to the quasi-steady forced state, which is shown in Figure 13j. This state is initial state for the $SS \rightarrow 0$ transition ($u_f = 1$), for which the flow is attached to the downstream edge of the actuator and along the airfoil to the trailing edge. Following the termination of *SS* actuation, the vorticity layer passing over the jet exit begins to detach from the Coanda surface (Figure 13k). As this vorticity layer pulls off the surface, a region of stagnant fluid develops at the juncture between the actuator and the airfoil surface at $x/c = (0.88, 0.04)$. The flow becomes fully separated at the trailing edge at $t = 0.46T_{conv}$ (Figure 13l) and keeps relaxing to the fully unforced state (Figure 13g) until nearly two convective time scales ($t = 1.96T_{conv}$).

The time scale associated with the actuation process is also assessed using a survey of the local vorticity flux $u\cdot\omega_z$ into the wake. Maps of the time-variation of phase-averaged cross stream distributions of $u\cdot\omega_z$ extracted from the PIV measurements at $x/c = 1.04$, following the transitions 0-*SS*, *SS*-0, *PS*-*SS,* and *SS*-*PS,* are shown in Figures 14a-d, respectively. Considering first the transition 0-*SS* (Figure 14a), the cross-stream flux distribution at $t = 0$ corresponds to the unactuated flow (cf. Figure 8b) in which the *SS* (CW) and *PS* (CCW) shear layers are separated by a cross-stream gap $\Delta y = 0.06c$ owing to the recirculation regions downstream of each actuator. A large CW vortex resulting from severing of the CW shear layer is evident for $0.2 < t/T_{conv} < 0.33$ at $0.03 < y/c < 0.09$. Following the passage of this vortex, there is momentary decrease in flux of CW vorticity from the suction surface ($0.33 < t/T_{conv} < 0.46$) as the circulation around the airfoil builds up (*SS* actuation is associated with an increase in C_L).

Following this period of net CCW vorticity flux, the wake relaxes to the $u_f = 1$ state which is nearly complete by $t = 0.8T_{conv}$. The transition *SS*-0 (Figure 14b) occurs over a slightly longer period. Starting at $u_f = 1$ at $t = 0$, the cross-stream width of the CW shear layer begins to diminish around $t = 0.4T_{conv}$ which is about the time that the separation along the *SS* surface of the airfoil reaches the trailing edge. During $0.46 < t/T_{conv} < 0.82$, the cross-stream width of the CCW (*PS*) shear layer diminishes as CW vorticity is transported into the wake and the circulation about the airfoil decreases. For $t/T_{conv} > 0.82$, the CCW shear layer thickens to its unforced state and the CW shear layer is advected in the cross-stream direction to its unforced elevation which is nearly reached by $t = 1.4T_{conv}$.

The vorticity flux map for the transition *PS*-*SS* is shown in Figure 14c, and demonstrates that the primary difference between 0-*SS* and *PS*-*SS* transitions is that in the latter there is more interaction between the CW and CCW shear layers because of their closer proximity during the initial state ($u_f = -1$, $\Delta y = 0.05c$). Immediately following the passage of the large CW vortex from the suction surface ($0.3 < t/T_{conv} < 0.43$), there is a period of strong CCW vorticity flux ($u \cdot \omega_z = 35 U_0^2$) during which the airfoil gains significantly more lift than following the transition 0-*SS* ($\Delta C_L = 0.34$ vs 0.14). A large contribution to this CCW vorticity flux is the large CCW vortex noted in connection with Figure 13. Finally, the local vorticity flux distribution following the transition *SS*-*PS* is shown in Figure 14d. The large CCW vortex resulting from the severing of the CCW shear layer by the onset of *PS* actuation (cf. Figure 13) is evident at $-0.04 < y/c < -0.02$ for $0.1 < t < 0.2$. Following the passage of this vortex, there is a period of diminished CCW vorticity flux from the *PS* side of the airfoil as the lift on the airfoil decreases by $\Delta C_L = -0.34$ (i.e., the difference between $u_f = 1$ and $u_f = -1$). The process is complete by $t = 1.4T_{conv}$

and for the remaining part of the record ($1.4 < t/T_{conv} < 1.94$) the flux profile corresponds to $u_f = -1$, which is characterized by a thinning of both the CW and CCW shear layers as well as an upward displacement of the latter.

The total vorticity flux from each side of the airfoil as well as the total net vorticity flux into the wake is computed at each time step by cross-stream integration:

$$\left(\frac{d\Gamma}{dt}\right)_{SS} = \int_{y_{wake}}^{y_{max}} u\omega_z dy$$

$$\left(\frac{d\Gamma}{dt}\right)_{PS} = \int_{y_{min}}^{y_{wake}} u\omega_z dy$$

$$\left(\frac{d\Gamma}{dt}\right)_{total} = \left(\frac{d\Gamma}{dt}\right)_{SS} + \left(\frac{d\Gamma}{dt}\right)_{PS}$$

where y_{min} and y_{max} are the lower and upper edges of PIV domain and y_{wake} is the 'wake center' defined by the vorticity zero-crossing at the streamwise survey point $x_0 = 1.04$. The extents of the PIV domain were selected such that ω_z vanished on both the upper and lower edges and thus these integrals converge. Note that the vorticity flux is averaged over a small streamwise domain ($\Delta x = 0.015c$) to improve measurement fidelity. Time histories of the normalized fluxes $(d\Gamma/dt)_{SS}/U_0^2$, $(d\Gamma/dt)_{PS}/U_0^2$, $(d\Gamma/dt)_{total}/U_0^2$ are plotted in Figure 15 for each of the four transitions in Figure 14. A prevailing feature is that the largest fluctuations in vorticity flux are seen on the side of the airfoil undergoing actuation transition. For example, in Figures 15a and b, only the *SS* actuator is transitioned and accordingly the variations in $(d\Gamma/dt)_{SS}$ are twice as large as those in $(d\Gamma/dt)_{PS}$. In these cases, the major changes in circulation about the airfoil are controlled by the intensification and diminution of vorticity flux from the transitioning side of

the airfoil while the flux from the opposing side varies on a much smaller scale. The largest excursion of $(\mathrm{d}\Gamma/\mathrm{d}t)_{\mathrm{total}}$ occurs during the transition *PS*-*SS* (Figure 15c) as the large CW vortex from the suction side at $t = 0.23T_{\mathrm{conv}}$ is immediately followed by the CCW vortex from the pressure side $t = 0.33T_{\mathrm{conv}}$. As these vortices pass, $\left(d\Gamma/dt\right)_{total}/U_0^2$ varies from -0.6 to 0.8.

The total vorticity flux $(\mathrm{d}\Gamma/\mathrm{d}t)_{\mathrm{total}}$ for each of the four transitions is integrated forward in time to obtain the time-history of circulation change $\Delta\Gamma$ about the airfoil. The normalized circulation change $\Delta\Gamma/(U_0 \cdot c)$ about the airfoil is plotted in Figure 16 (positive circulation corresponds to positive lift). Along with the transient $\Delta\Gamma$, the steady change in circulation corresponding to the measured change in lift is also plotted (solid line). For the 0-*SS* transition (Figure 16a), the airfoil experiences a slight decrease in circulation during $0.23 < t/T_{\mathrm{conv}} < 0.3$ as the CW vortex passes, followed by a monotonic increase to the steady state value for $t > 0.3T_{\mathrm{conv}}$. Conversely, during *SS*-0 transition the circulation first exhibits a slight increase ($0.26 < t/T_{\mathrm{conv}} < 0.46$) followed by a monotonic decrease towards the steady state value (Figure 16b). The trend of $\Delta\Gamma$ for *PS*-*SS* transition (Figure 16c) is qualitatively similar to that of the 0-*SS* transition; however, the initial decrease and subsequent increase in circulation are larger in magnitude owing to the larger fluxes of vorticity discussed in connection with Figure 15c. However, the *SS*-*PS* transition exhibits a rather different $\Delta\Gamma$ trend than any of the other three cases (Figure 16d). Initially, $\Delta\Gamma$ exhibits a slight increase as the CCW vortex passes ($0.1 < t/T_{\mathrm{conv}} < 0.16$). As the flux from the pressure side of the airfoil abates ($0.16 < t/T_{\mathrm{conv}} < 0.23$), $\Delta\Gamma$ decreases to zero (Γ returns to its initial value). For $0.23 < t/T_{\mathrm{conv}} < 0.49$, the diminished flux from the pressure side is approximately balanced by the diminished flux from the suction side and as a result $\Delta\Gamma$ nearly vanishes (cf. Figure 15d). Finally at $t = 0.5T_{\mathrm{conv}}$, the vorticity flux from the suction side resumes

and $\Delta\Gamma$ steadily decreases for $0.5 < t/T_{conv} < 0.9$. For $t > 0.9T_{conv}$, the flux from the suction side remains invariant while the flux from the pressure side increases until the total flux into the wake vanishes. Consequently, the circulation relaxes to the steady-state value.

6. Concluding Remarks

The present investigations explored the utilization of trapped vorticity near the trailing edge of an airfoil at low angles of attack, when the flow is fully attached, for modification of its global circulation. Trapped vorticity is engendered and regulated by small surface protrusions that include synthetic jet actuators to realize hybrid flow control. The actuators are mounted on both the suction and pressure surfaces of a static airfoil (*SS* and *PS*, respectively) upstream of the trailing edge, and their nominally quasi-steady and transient effects (at the onset and termination of the actuation) are explored in wind tunnel experiments over a range of angles of attack ($-5° < \alpha < 15°$). In these investigations the streamwise location of the actuator was varied within the range $0.83 < x/c < 1$, and the normalized modulation amplitude of the actuator's resonance waveform was varied between 0 and 1 on each surface.

Time-averaged PIV measurements about the airfoil's trailing edge in the absence and presence of quasi steady actuation showed that operation of either actuator over a range of momentum coefficients results in reduction of the trapped vorticity domain downstream of the actuator. The effects of these changes in the vorticity concentrations are accompanied by changes in the local static pressure distribution, which are associated with changes in the pitching moment and to a lesser extent in the lift. Furthermore, the reduction (or partial collapse) of the trapped vorticity domain leads to vectoring of the flow downstream of the actuator towards the airfoil and thereby to significant changes in the trailing edge Kutta condition as manifested by the migration of the

stagnation point from the near wake onto the surface of the airfoil. The performance of the *PS* and *SS* actuators could be optimized to effect changes in pitching moment as large as $\Delta C_M = -0.05$ (nose-down) and 0.09 (nose-up) that corresponds to 140% of the pitching moment of the base airfoil ($C_M = -0.1$) at $\alpha = 3°$.

The transient response of the flow to time-dependent (step) modulation of the actuation waveform was investigated to determine the characteristic time scales that are associated with the onset and termination of the actuation. Time-resolved, transitory surface pressure measurements are recorded following transitions from three states, namely, unactuated ($u_f = 0$), full *SS* actuation ($u_f = 1$), and full *PS* actuation ($u_f = -1$). It is found that the surface pressure near the trailing edge adjusts to the quasi-steady level of continuous actuation within one to two convective time scales ($T_{conv} = c/U_0 = 15$ ms), while the pressure closer to the leading edge ($0 < x/c < 0.4$) reaches the quasi-steady levels within $2 - 4T_{conv}$. From the standpoint of a flight control system, the present measurements indicate an operational bandwidth of about 16 Hz.

The transient dynamics of vorticity concentrations following the onset and termination of actuation were further characterized using phase-locked PIV measurements. During the onset of actuation, the first counter-rotating vortex pair formed by the synthetic jet causes the separated shear layer to roll up into a large vortex (nominally $0.03c$) which is advected into the wake. For the step-modulated transition from unforced flow to full *SS* actuation ($0 \rightarrow SS$), this vortex has clockwise (CW) sense and corresponds to a momentary decrease in C_L (as the total circulation about the airfoil decreases) and increase in C_M. Following the advection of this vortex, the upstream shear layer becomes attached to the Coanda surface downstream of the jet exit. During this attachment, the vorticity flux from the suction surface of the airfoil is temporarily abated

indicating accumulation and eventual increase in circulation (and lift). For the corresponding transition $0 \rightarrow PS$, counter-clockwise (CCW) vorticity is initially shed from the pressure side of the airfoil, and the total circulation about the airfoil momentarily increases above the initial circulation (in the absence of actuation). This is followed by a period of net CW vorticity flux as the flow attaches around the *PS* actuator and the total circulation around the airfoil decreases to a value which corresponds to the C_L decrease associated with the *PS* actuators. When actuation is terminated, the vorticity layer on the surface of the airfoil slowly lifts off the surface (over a period of $0.5T_{conv}$), starting at the juncture between the downstream edge of the actuator and the surface of the airfoil. The lift-off process is accompanied by a momentary reduction in vorticity flux from the same side of the airfoil. For example, during the transition $0 \rightarrow SS$ there is a momentary increase in circulation about the airfoil, and, consequently, in C_L. However, once the separation progresses to the trailing edge, the vorticity flux changes sign because much of the vorticity associated with the previously-attached surface layer is shed into the wake. It is noteworthy that for both onset and termination of actuation, the changes in vorticity flux are almost exclusively confined to the actuated surface of the airfoil.

The present work demonstrated that the trapped vorticity actuation effected near the trailing edge of the airfoil offers the potential for agile maneuvering when the flow is fully attached. In addition to maneuvering in the absence of mechanical control surfaces, this flow control approach has the potential to enable novel wing designs that currently might be hindered by limitations of conventional control surfaces.

Acknowledgement

This research was supported by the U.S. Air Force Office of Scientific Research (AFOSR grant FA9550-05-1-0411) and the Multidisciplinary University Research Initiative.

References

Ahuja, K. H. & Burrin, R. H. 1984 Control of flow separation by sound. *AIAA Paper* 84-2298.

Amitay, M. & Glezer, A. 2002a Controlled transients of flow reattachment over stalled airfoils. *Int. J. Heat Fluid Flow* **23**, 690–699.

Amitay, M. & Glezer, A. 2002b Role of actuation frequency in controlled flow reattachment over a stalled airfoil. *AIAA J.* **40**, 209–216.

Amitay, M. & Glezer, A. 2006 Flow transients induced on a 2d airfoil by pulse-modulated actuation. *Exp. Fluids* **40**, 329–331.

Amitay, M., Horvath, M., Michaux, M. & Glezer, A. 2001 Virtual aerodynamic shape modification at low angles of attack using synthetic jet actuators. *AIAA Paper* 2001–2975.

Brzozowski, D. P. 2011 Dynamic control of aerodynamic forces on a moving platform using active flow control. *Ph.D. Thesis*, Georgia Institute of Technology.

Brzozowski, D. P., Woo, G. T. K., Culp, J. R. & Glezer, A. 2010 Transient separation control using pulse-combustion actuation. *AIAA J.* **48**, 2482–2490.

Buchmann, N.A., Atkinson, C. & Soria, J. 2013. Influence of ZNMF jet flow control on the spatio-temporal flow structure over a NACA-0015 airfoil. *Exp. Fluids* **54**:1485.

Cattafesta, L., Tian, Y. & Mittal, R. 2009. Adaptive control of post-stall separated flow application to heavy vehicles. In *The Aerodynamics of Heavy Vehicles II: Trucks, Buses, and Trains*, pp. 151-160, Springer, Berlin, Heidelberg.

Cox, J. 1973 The revolutionary Kasper wing. *Soaring* **37**, 20-23.

Crittenden, T. & Glezer, A. 2006 A high-speed, compressible synthetic jet. *Phys. Fluids* **18**, 017107.

Darabi, A. & Wygnanski, I. 2004a Active management of naturally separated flow over a solid surface. Part 1. The forced reattachment process. *J. Fluid Mech.* **510**, 105–129.

Darabi, A. & Wygnanski, I. 2004b Active management of naturally separated flow over a solid surface. Part 2. The separation process. *J. Fluid Mech.* **510**, 131–144.

DeSalvo, M. E. & Glezer, A. 2004 Aerodynamic performance modification at low angles of attack by trailing edge vortices. *AIAA Paper* 2004–2118.

DeSalvo, M. E. & Glezer, A. 2005 Airfoil aerodynamic performance modification using hybrid surface actuators. *AIAA Paper* 2005-0872.

DeSalvo, M. E. & Glezer, A. 2007 Control of airfoil aerodynamic performance using distributed trapped vorticity. *AIAA Paper* 2007-0708.

Feng, L.H., Choi, K.S. & Wang, J.J. 2015 Flow control over an airfoil using virtual Gurney flaps. *J. Fluid Mech.* **767**, 595–626.

Funk, R., Parekh, D. E., Crittenden, T. & Glezer, A. 2002 Transient separation control using pulse actuation. *AIAA Paper* 2002–3166.

Glezer, A., Amitay, M., & Honohan, A. M. 2005 Aspects of low- and high-frequency actuation for aerodynamic flow control. *AIAA J.* **43**, 1501-1511.

Greenblatt, D. & Wygnanski, I.J. 2000. The control of flow separation by periodic excitation. *Prog. Aerosp. Sci.* **36**, 487–545.

Greenblatt, D. 2006 Managing flap vortices via separation control. *AIAA J.* **44**, 2755–2764.

Honohan, A. M., Amitay, M. & Glezer, A. 2000 Aerodynamic control using synthetic jets. *AIAA Paper* 2000-2401.

Hsiao, F.-B., Liu, C.-F. & Shyu, J.-Y. 1990 Control of wall-separated flow by internal acoustic excitation. *AIAA J.* **28**, 1440–1446.

Hurley, D.G. 1959 The use of boundary-layer control to establish free stream-line flows. *Adv. Aeronaut. Sci.* **2**, 662-708.

Liebeck, R. H. 1978 Design of subsonic airfoils for high lift. *J. Aircraft* **15**, 547–561.

Mathis, R., Lebedev, A., Collin, E., Delville, J. & Bonnet, J.-P. 2009 Experimental study of transient forced turbulent separation and reattachment on a bevelled trailing edge. *Exp. Fluids* **46**, 131–146.

Nishri, B. & Wygnanski, I. 1998. Effects of periodic excitation on turbulent flow separation from a flap. *AIAA J.* **36**, 547–556.

Perkins, C.D. & Hazen, D. 1953 Some recent advances in boundary layer and circulation control. *Proc. of the 4th Anglo-American Aeronautical Conference*. London, U.K.

Raffel, M., Willer, C. E., Wereley, S. T. & Kompenhans, J. 2007 *Particle Image Velocimetry.* Springer.

Roshko, A. 1993 Perspectives on bluff body aerodynamics. *J. Wind Eng. Ind. Aerod.* **49**, 79–100.

Rossow, V.J., 1978 Lift enhancement by an externally trapped vortex. *J. Aircraft* **15**, 618-625.

Saffman, P.G. & Sheffield, J.S. 1977. Flow over a wing with an attached free vortex. *Stud. Appl. Math.* **57**, 107-117.

Seifert, A., Bachar, T., Koss, D., Shepshelovich, M. & Wygnanski, I. 1993 Oscillatory blowing: A tool to delay boundary-layer separation. *AIAA J.* **31**, 2052–2060.

Shea, P. & Smith, D. 2009. Aerodynamic control of a rectangular wing using gurney flaps and synthetic jets. *AIAA Paper* 2009-886.

Siauw, W.L. & Bonnet, J.P. 2017 Transient phenomena in separation control over a NACA 0015 airfoil. *Int. J. Heat Fluid Fl.* **67**, 23-29.

Siauw, W.L., Bonnet, J.P., Tensi, J., Cordier, L., Noack, B.R. & Cattafesta, L. 2010 Transient dynamics of the flow around a NACA 0015 airfoil using fluidic vortex generators. *Int. J. Heat Fluid Fl.* **31**, 450-459.

Smith, A.M. 1975. High-lift aerodynamics. *J. Aircraft* **12**, 501–530.

Timor, I., Ben-Hamou, E., Guy, Y. & Seifert, A. 2007 Maneuvering aspects and 3d effects of active airfoil flow control. *Flow Turbul. Combust.* **78**, 429-443.

Traub, L.W. & Agarwal, G. 2008 Aerodynamic characteristics of a Gurney/jet flap at low Reynolds numbers. *J. Aircraft* **45**, 424–429.

Watson, M., Jaworski, A. J. & Wood, N. J. 2007 Application of synthetic jet actuators for the modification of the characteristics of separated shear layers on slender wings. *Aeronaut. J.* **111**, 519–529.

Woo, G.T.K. & Glezer, A. 2013 Controlled transitory stall on a pitching airfoil using pulsed actuation. *Exp. Fluids* **54**: 1507.

Wu, J.-Z., Lu, X.-Y., Denny, A. G., Fan, M. & Wu, J.-M. 1998 Post stall flow control on an airfoil by local unsteady forcing. *J. Fluid Mech.* **371**, 21–58.

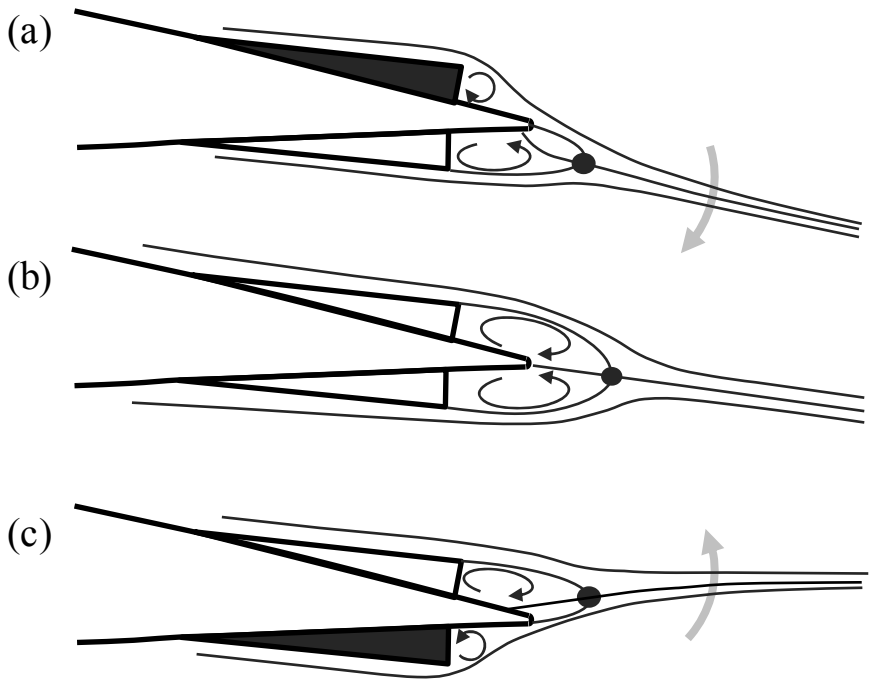

Figure 1. Conceptual bi-directional control of a pitching moment by hybrid formation and control of trapped vorticity at suction (*a*) and pressure (*c*) side of an airfoil tail. Passive formation of trapped vorticity is shown in (*b*).bvg

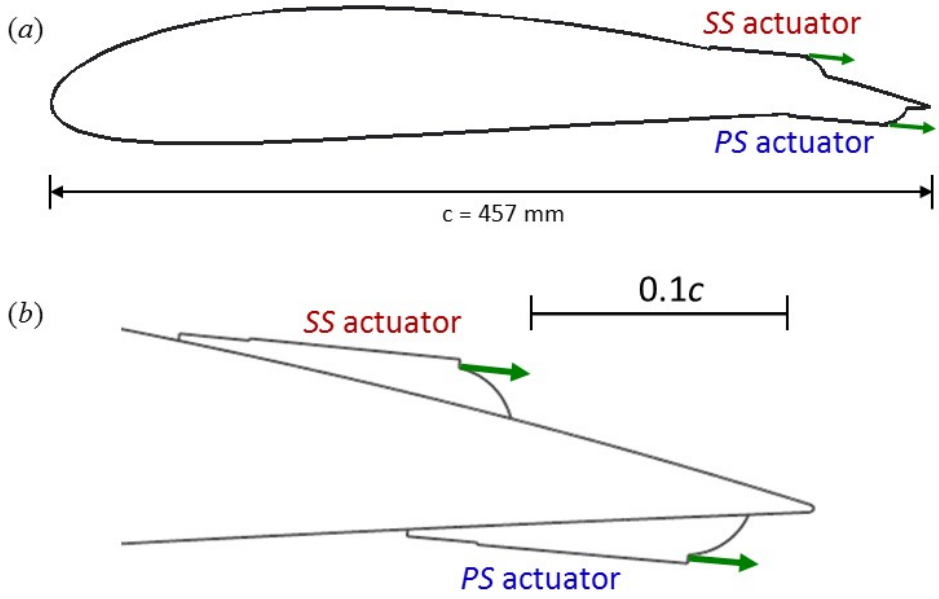

Figure 2. NACA4415 airfoil with modified profile geometry near the trailing edge (*a*), and a close-up of the trailing edge region (*b*).

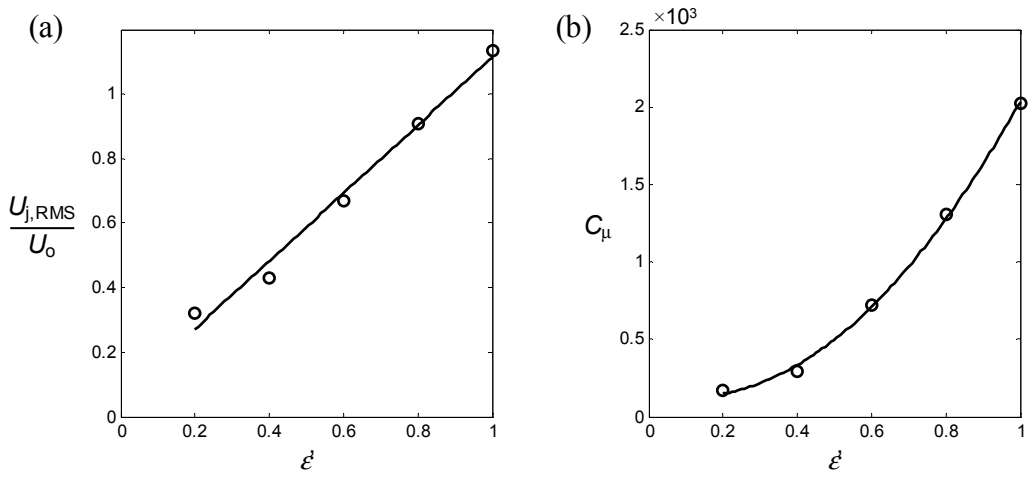

Figure 3. Synthetic jet calibration: variation of RMS jet velocity (*a*) and momentum coefficient (*b*) at the center of the jet orifice with the jet power fraction ε'.

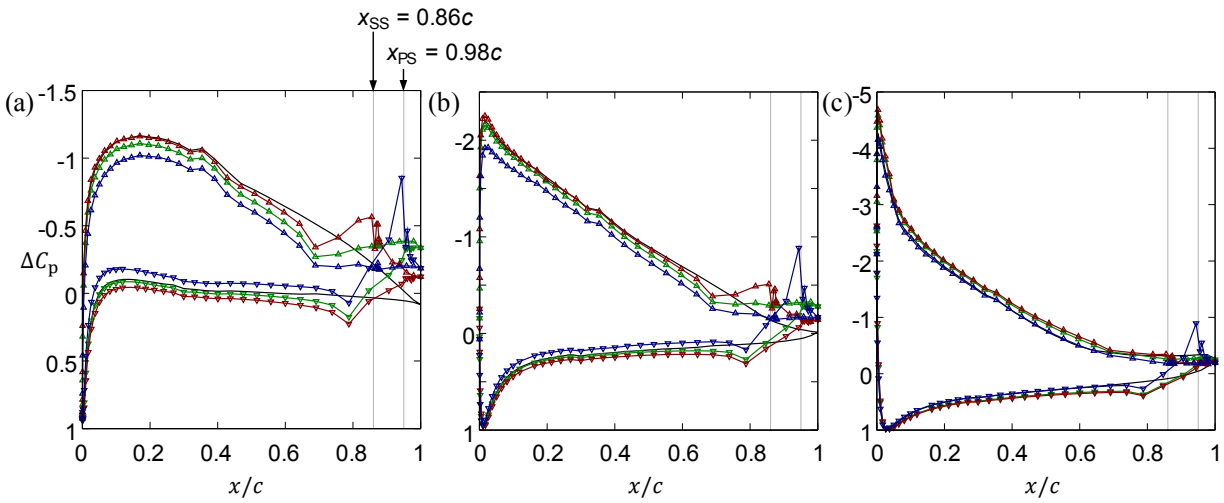

Figure 4. Distributions of static pressure Cp when the actuators are mounted at [x_{SS} = 0.86c, x_{PS} = 0.95c] for α = 3◦ (a), 9◦ (b), and 15◦ (c), and actuation level u_f = 0 (▲), 1 (▲), and −1 (▲). Corresponding C_p for the smooth airfoil (-).

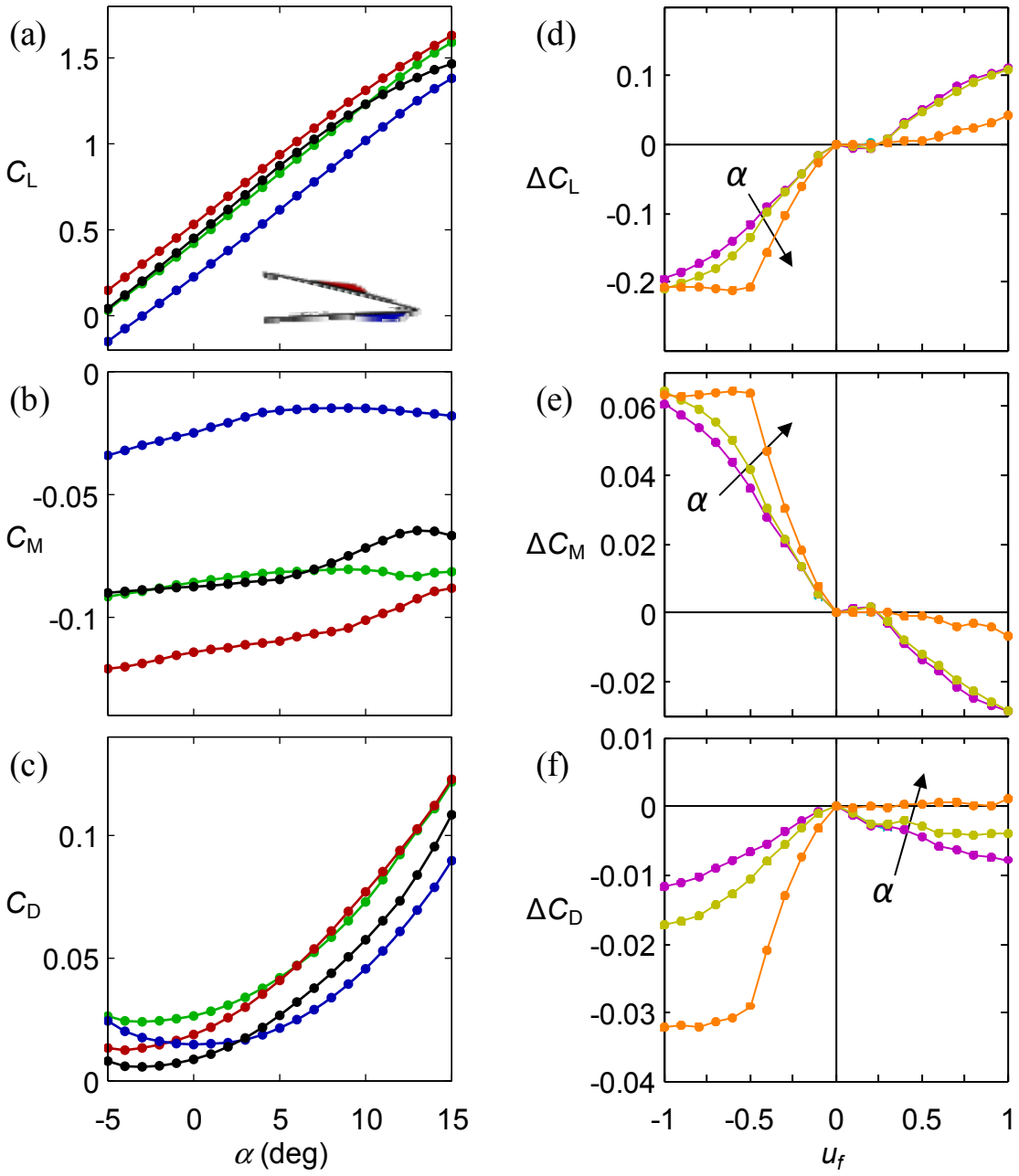

Figure 5. Variation of C_L (*a*), C_M (*b*), and C_D (*c*) with α for the smooth airfoil (•) and modified [x_{SS} =0.86c, x_{PS} = 0.95c] airfoil with u_f = 0 (•), 1 (•), and -1 (•). Variation of ΔC_L (*d*), ΔCM (*e*), and ΔC_D (*f*) with u_f for α = 0° (•), 3° (•), and 15° (•).

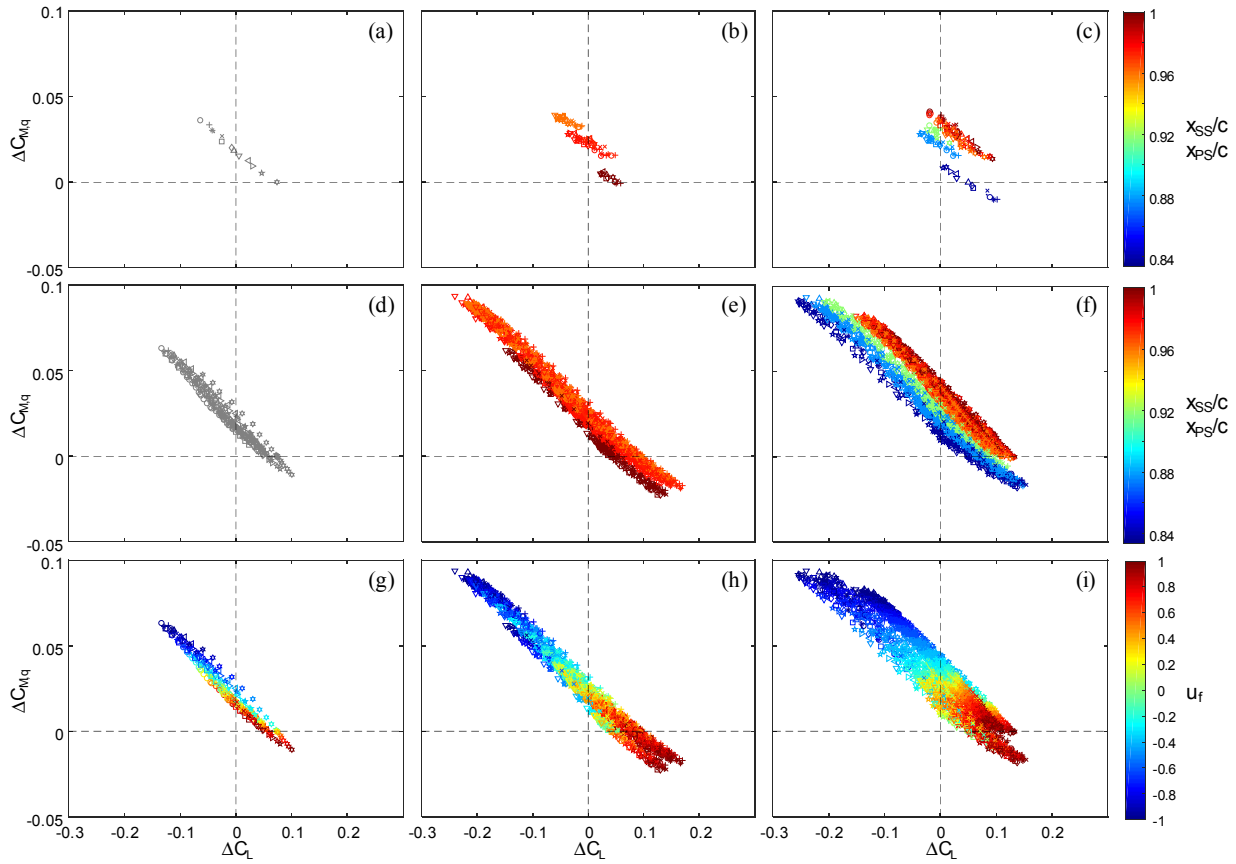

Figure 6. Variation of ΔC_M with $\Delta C_{L,}$ [relative to the base (smooth) airfoil] in the presence of the inactive (a-c) and active ($-1 < u_f < 1$, d-i) actuation: ***i***. *(a, d, g)* the *SS* and *PS* actuators are flush with the airfoil's trailing edge; ***ii.*** *(b, e, f)* the *SS* actuator is fixed at $x_{SS} = 0.88c$ and the *PS* actuators is moved within $0.96c < x_{PS} < c$; ***iii.*** *(c, f, i)* the *PS* actuator is fixed at $x_{SS} = 0.98c$ and the *SS* actuators is moved within $0.83c < x_{SS} < c$. The data in (b, c, e, f) are colored by the position of the moving actuators, and the data in (e, f, h, i) are colored by the magnitude of the actuation.

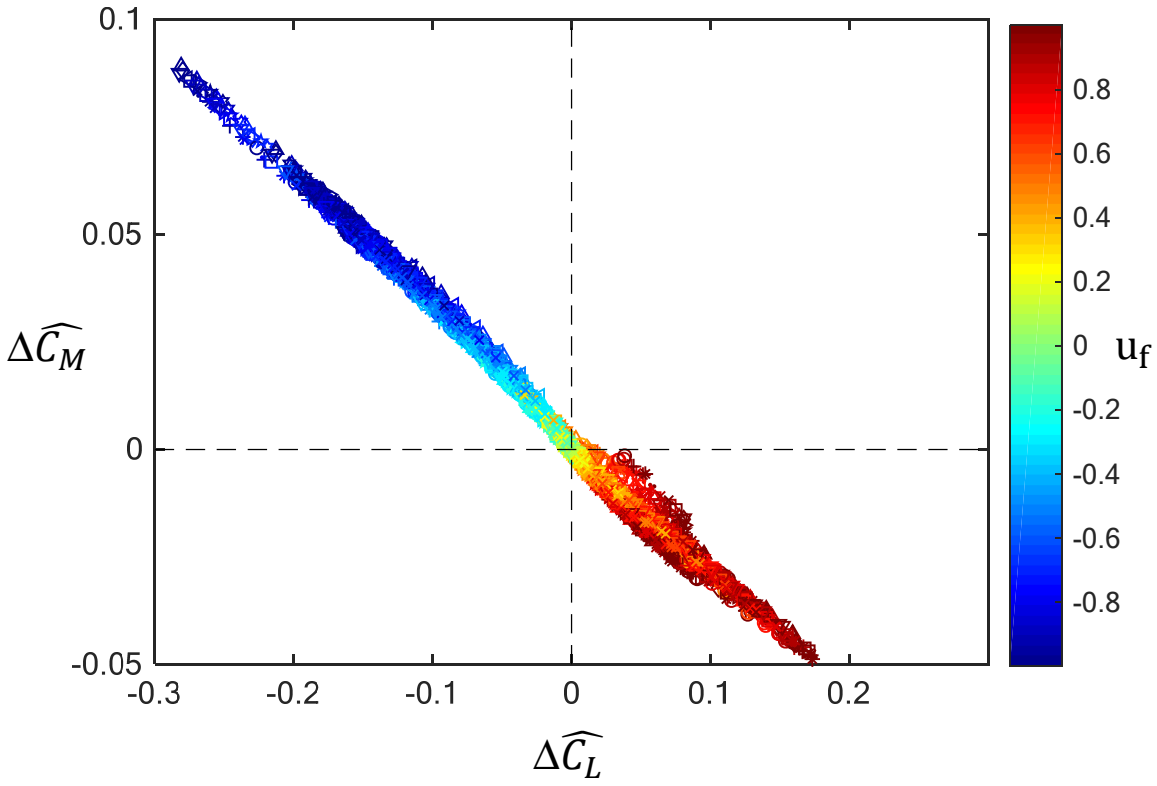

Figure 7. Variation of $\Delta\widehat{C_M}$ with $\Delta\widehat{C_L}$ for all the test cases: $0.83 < x_{SS} < 1$, $0.96 < x_{PS} < 1$, $-5° < \alpha < 15°$, and $-1 < u_f < 1$.

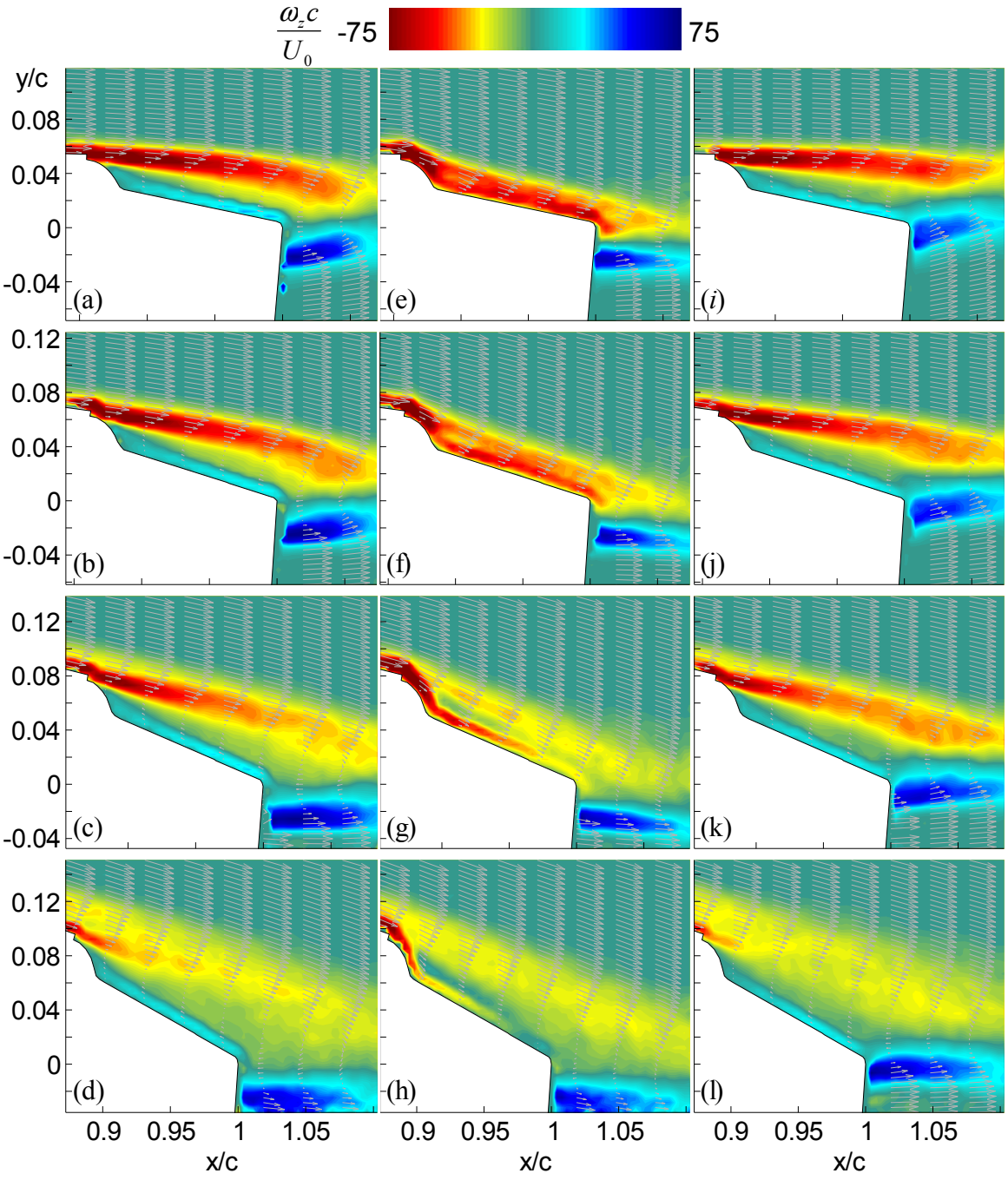

Figure 8. Raster plots of the time-averaged spanwise vorticity $\omega_z c/U_o$ at α = -3° (a,e,i), 3° (b,f,j), 9° (c,g,k), and 15° (d,h,l) with u_f = 0 (a-d), 1(e-h), and -1 (i-l).

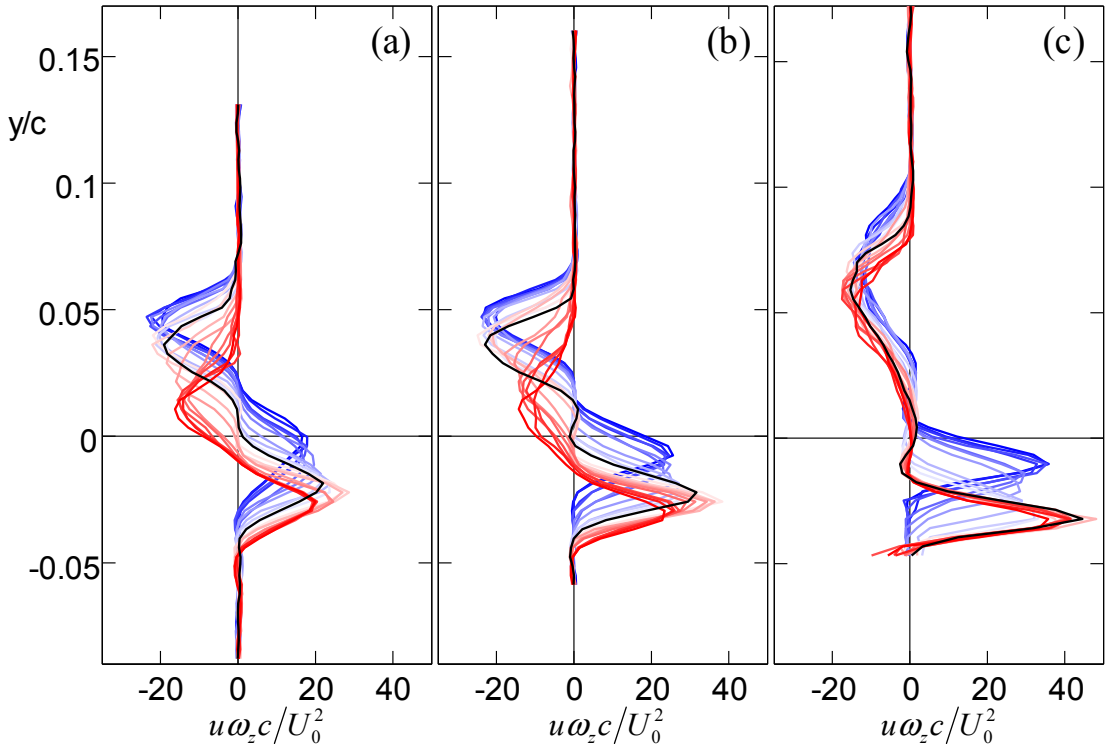

Figure 9. Time-averaged cross-stream distributions of vorticity flux in the wake (x/c = 1.05) for -1 <u_f < 1 for static model at α = -5° (a), 3° (b), and 15° (c). The traces are colored such black corresponds to the unactuated flow and increasing levels of red (blue) correspond to increasing levels of *SS* (*PS*) actuation.

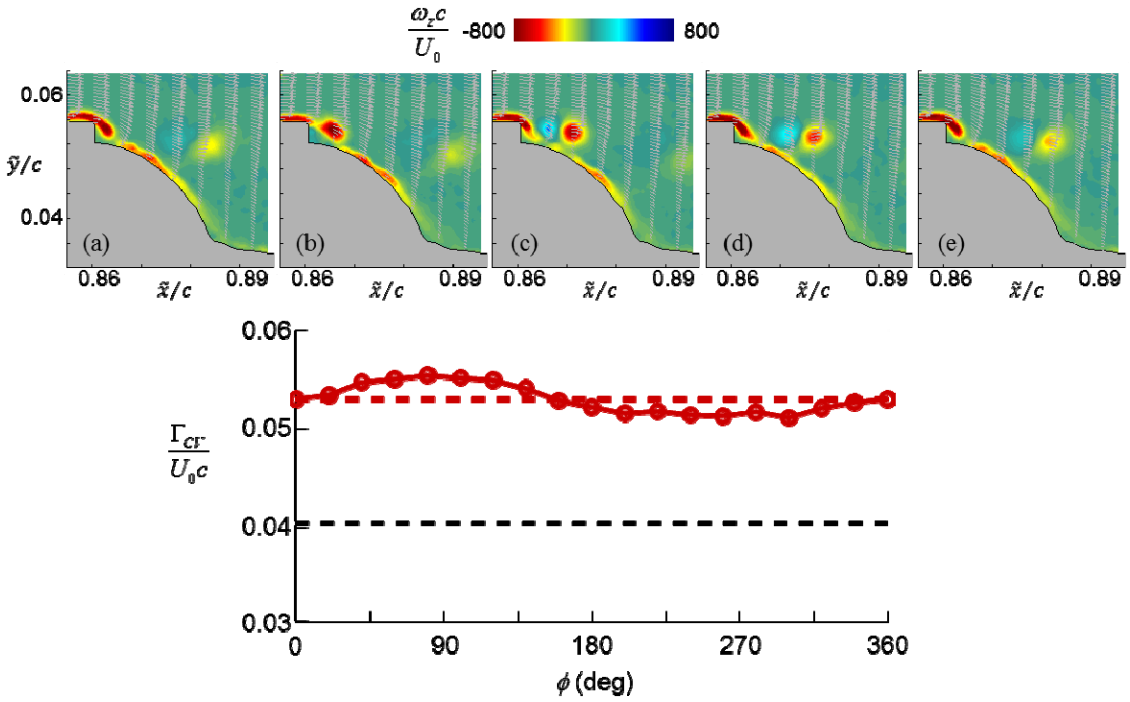

Figure 10. Raster plots of phase-averaged spanwise vorticity during the cycle of the synthetic jet at $\phi = 0°$ (a), 80° (b), 160° (c), 240° (d), and 320° (e), and the corresponding time history of circulation within the domain. Dashed lines indicate time-averaged circulation when $u_f = 0$ (black) and $u_f = 1$ (red).

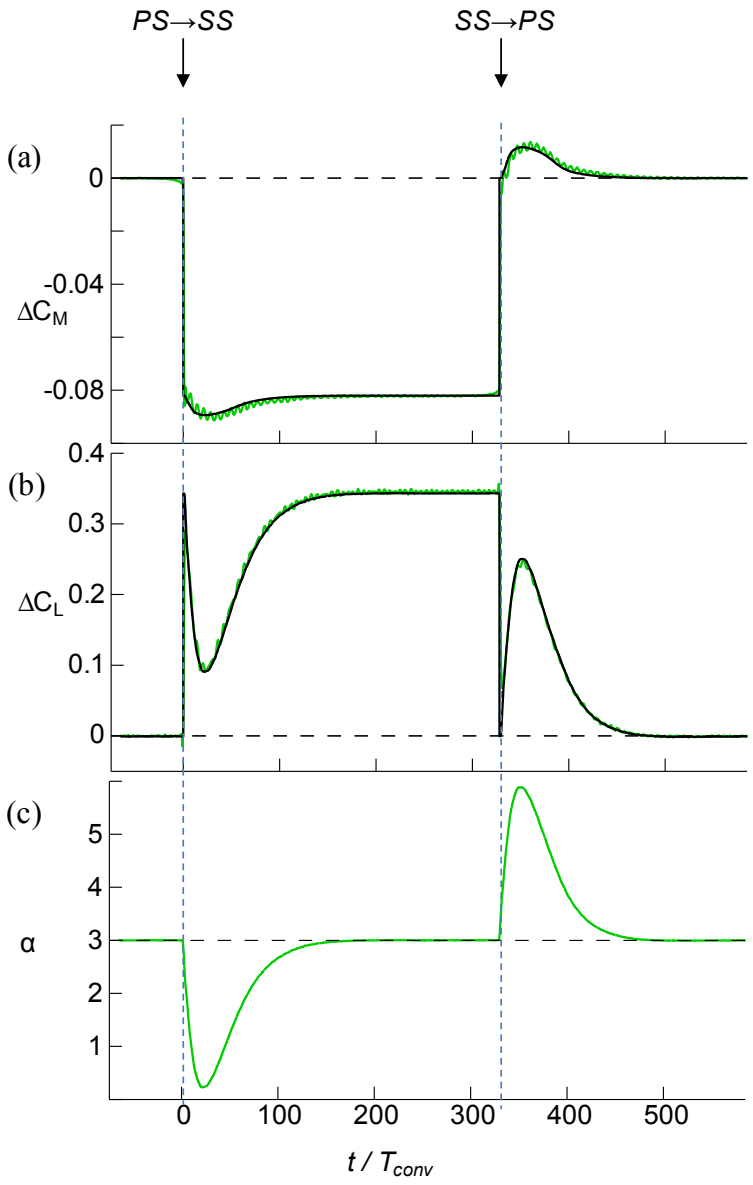

Figure 11. Time histories of α (*a*), ΔC_L (*b*), and ΔC_M (*c*) during step changes in actuation between SS and PS actuators. Black traces indicate corresponding steady-state values based on a look up table using α and u_f.

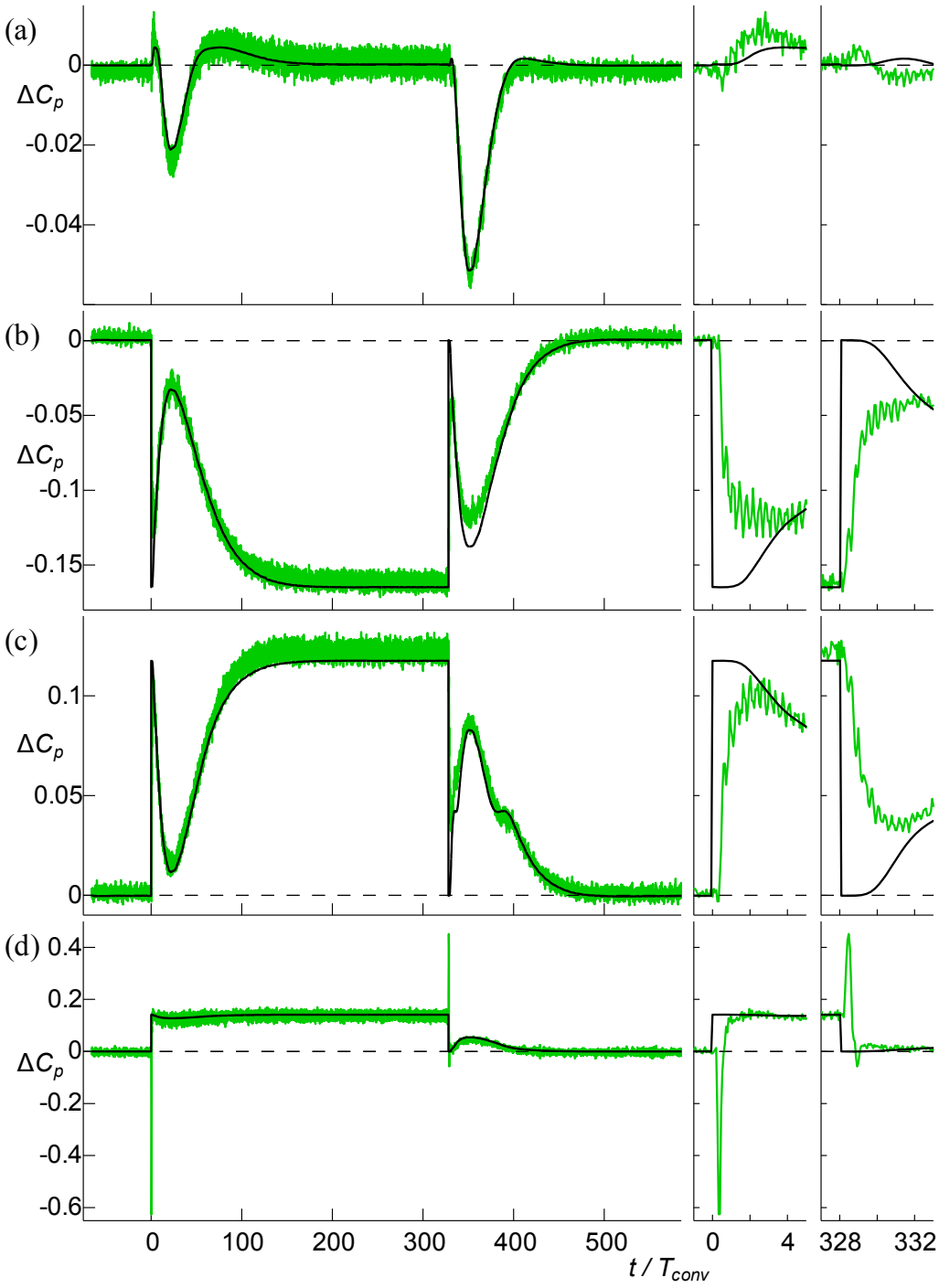

Figure 12. Time histories of ΔC_p at the leading edge (*a*), on the suction surface at $x/c = 0.39$ (*b*), on the pressure surface at $x/c = 0.4c$ (*c*), and at the trailing edge (*d*), with corresponding static values.

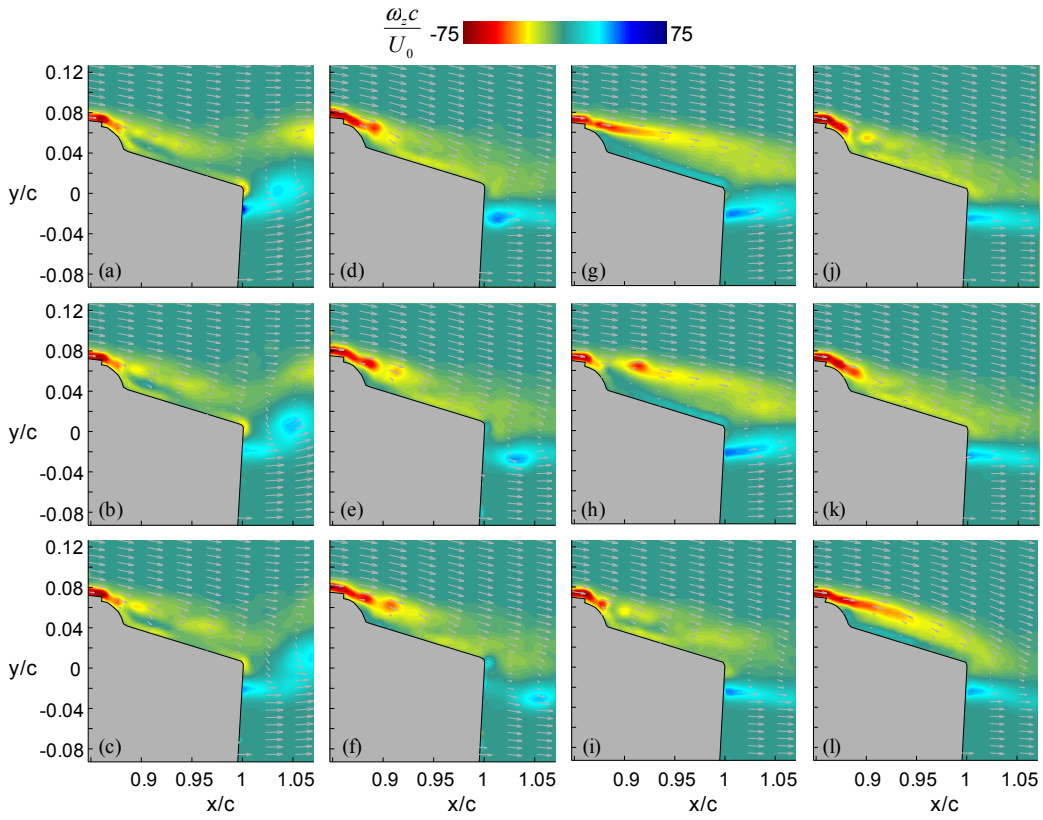

Figure 13. Raster plots of phase-averaged spanwise vorticity following actuation transitions at t/T_{conv} = 0.3, 0.33, and 0.36: *PS-SS* (a – c), and *SS-PS* (d – f), and at t/T_{conv} = 0, 0.07, and 0.46: *0-SS* (g – i), and *SS-0* (j – l).

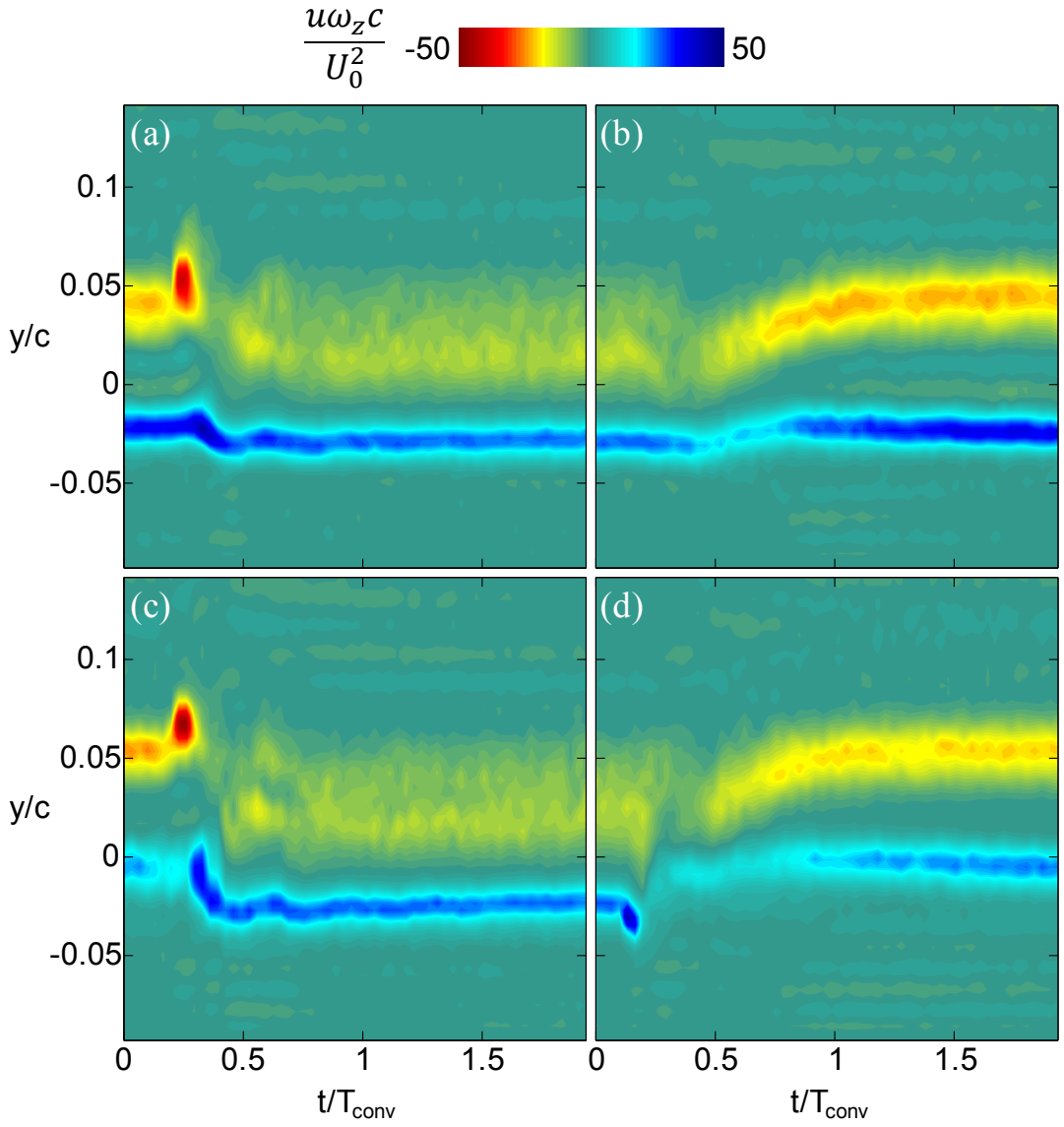

Figure 14. Color raster plots of time variation of the cross stream vorticity flux at $x/c = 1.04$ following transitions 0-*SS* (*a*), *SS*-0 (*b*), *PS*-*SS* (*c*), and *SS* -*PS* (*d*).

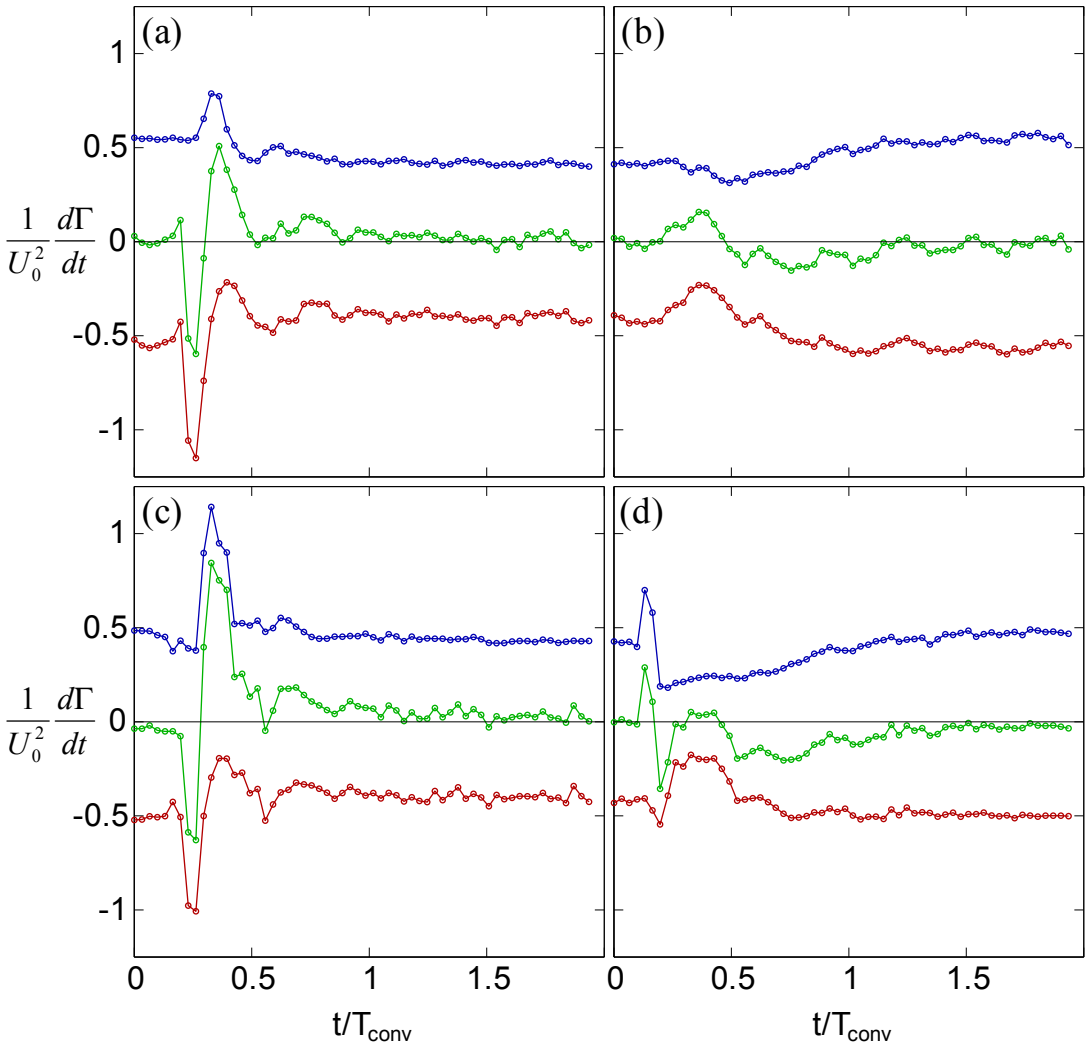

Figure 15. Respective time histories of vorticity flux of the four actuation transitions in Figure 14. Vorticity flux from suction and pressure sides of the airfoil is computed separately (red and blue traces, respectively). The total flux is shown in green.

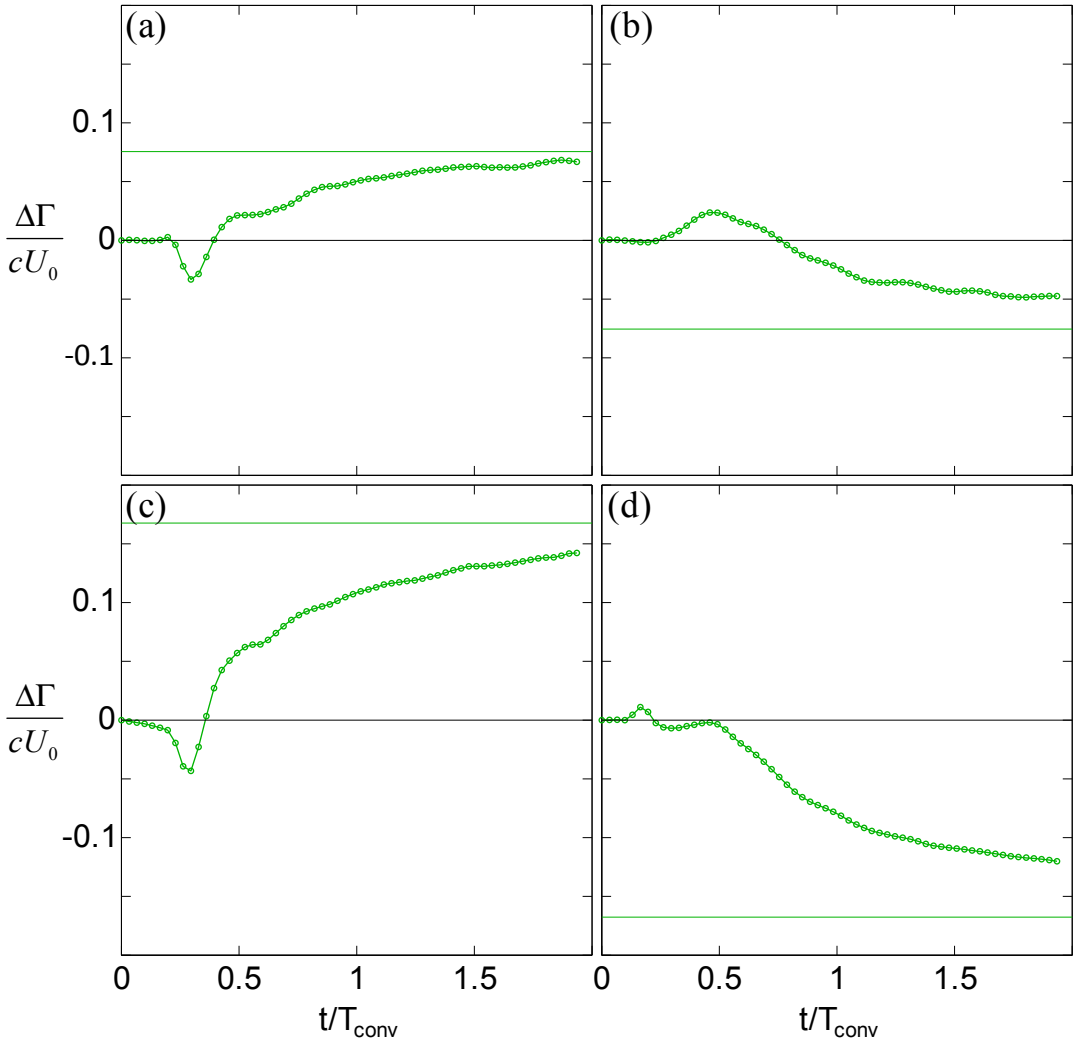

Figure 16. Time histories of the changes in circulation about the airfoil corresponding to the four actuation transition in Figure 14.